**Article:**
Santos, I.A., Fontes, J.V., Rodrigues, G.C. et al. (2025) Cu(I)-N-Heterocyclic carbenes as potent inhibitors of SARS-CoV-2 replication. BioMetals. ISSN: 0966-0844

https://doi.org/10.1007/s10534-025-00775-6

# Cu(I)-N-HETEROCYCLIC CARBENES AS POTENT INHIBITORS OF SARS-COV-2 REPLICATION

Igor Andrade Santos [a,b], Josielle V. Fontes [c], Gustavo C. Rodrigues [c], Mariana Ortiz de Godoy[d], Glaucius Oliva[d], Rafael V. C. Guido[d], Andres Merits [e], Camilla Abbehausen [c], Mark Harris [b]* and Ana Carolina Gomes Jardim [a,f,]*

[a] Institute of Biomedical Sciences, Federal University of Uberlândia, Brazil
[b] School of Molecular and Cellular Biology, Faculty of Biological Sciences, University of Leeds, UK
[c] Institute of Chemistry, University of Campinas, Brazil
[d] Instituto de Física de São Carlos, Universidade de São Paulo, São Carlos, Brazil
[e] Institute of Bioengineering, University of Tartu, Tartu, Estonia.
[f] Institute of Biosciences, Humanities and Exact Sciences, São Paulo State University, Brazil
*Corresponding authors

**Corresponding authors**
Professor Ana Carolina Gomes Jardim, Institute of Biomedical Science (ICBIM), Federal University of Uberlandia (UFU), Avenida Amazonas, 4C- Room 216, Umuarama, Uberlândia, Minas Gerais, Brazil, CEP: 38405-302
Tel: +55 (34) 3225-8682
E-mail: jardim@ufu.br

Professor Mark Harris, Faculty of Biological Sciences and Centre for Structural Molecular Biology, University of Leeds, Leeds, United Kingdom, LS2 9JT
Tel: +44(0)113 343 5632
E-mail: m.harris@leeds.ac.uk

## ABSTRACT

SARS-CoV-2 still poses as a threat to health systems despite the vaccination and the use of emergency repurposed drugs. Therefore, the development of novel anti-SARS-CoV-2 compounds is still needed. Organometallic copper(I)-N-heterocyclic carbenes [Cu(NHC)] are a class of metallodrugs that hold promise for drug development due to their variety of geometries, charges, and ligand design. Here we evaluated the activity of Cu(IPr)Cl, Cu(IMes)Cl, and $[Cu(IMes)_2]BF_4$ molecules against SARS-CoV-2 infection. Through a dose-response assay using A549-AT cells and the SARS-CoV-2-Wuhan infectious clone expressing mNeonGreen (SARS-CoV-2-mNeonGreen), Cu(IPr)Cl, Cu(IMes)Cl, and $[Cu(IMes)_2]BF_4$ inhibited SARS-CoV-2 replication with a selectivity index (SI) of 11.23, 10.84, and 5.94, respectively. The complexes Cu(IMes)Cl and $[Cu(IMes)_2]BF_4$ inhibited all stages of viral replication (pretreatment: 99.9% and 87.7%, entry: 99.6% and 74%, post-entry steps: 99.6% and 87.6%, respectively), while Cu(IPr)Cl impaired only entry (48%) and post-entry steps (95%). In addition, Cu(IMes)Cl and $[Cu(IMes)_2]BF_4$ complexes decreased the titres of both Delta and Omicron variants, while Cu(IPr)Cl only inhibited Omicron. In addition, $[Cu(IMes)_2]BF_4$ was able to decrease cell to cell spread of SARS-CoV-2; and for Cu(IMes)Cl a strong interaction with $PL^{pro}$ was revealed. Based on this data further investigations of Cu(I) based organometallics are warranted and Cu(IPr)Cl and Cu(IMes)Cl may be considered for utilization in pre-clinical assays.

**Keywords:** Antivirals, Copper complexes, Organometallic compounds, SARS-CoV-2

## 1. INTRODUCTION

The Coronavirus Disease 2019 (COVID-19) pandemic, caused by *Severe Acute Respiratory Syndrome Coronavirus 2* (SARS-CoV-2), a positive single-stranded RNA virus from the *Coronaviridae*, highlighted the urgency of developing antiviral agents against current and future viral outbreaks (Zhang et al. 2020; Shi et al. 2020; von Delft et al. 2023). Notably, as other RNA viruses, SARS-CoV-2 has displayed high potential to genetic variability, contributing to the rapid emergence of global variants, including the Variants of Concern (VOCs) such as Alpha, Beta, Gamma, Delta, and Omicron (Duffy 2018; Montagutelli et al. 2021; Wang et al. 2021; Thakur and Ratho 2021; Johnson et al. 2022).

SARS-CoV-2 has a higher transmission rate than other respiratory viruses, which facilitated its worldwide spread (Grasselli et al. 2020; Lamers and Haagmans 2022). In humans, SARS-CoV-2 infection can cause moderate to severe illness, related to upper and lower respiratory tract infection, that can develop into a severe acute respiratory syndrome (SARS) and lead to death. Additionally, even after vaccination, COVID-19 patients can develop long-lasting chronic symptoms described as the Post-COVID Syndrome or Long-COVID, directly impacting their quality of life (Oronsky et al. 2021; Maltezou et al. 2021a, b; Augustin et al. 2021; Yong 2021).

So far, there are only a few drugs licenced for the treatment of COVID-19, such as remdesivir, molnupiravir, and Paxlovid® (nirmatrelvir, ritonavir) (Saúde. 2022; Jayk Bernal et al. 2022; Liu et al. 2023; Pantazis et al. 2023). The shortage of approved drugs against SARS-CoV-2 associated with the rapid resistance of omicron variants against Paxlovid and molnupiravir emphasizes the necessity for a diverse array of therapeutic approaches capable of abrogating viral infection (Sanderson et al. 2023). Therefore, the development of new molecules that are effective against RNA viruses can provide novel important insights to combat these viruses and prepare health researchers for future outbreaks caused by emerging viruses.

The coordination or organometallic compounds are organic or inorganic molecules bound with a metal ion (Messerschmidt et al. 2004; de Paiva et al. 2020; Boros et al. 2020), and possess chemical and structural attributes that cannot be solely replicated by organic motifs, making them a promising and versatile avenue for drug development (Karlin 1993; Shahabadi et al. 2012; Zoroddu et al. 2019; de Paiva et al. 2020; Boros et

al. 2020). Among the metal ions, copper (Cu) is an essential element in mammalians cells, and therefore is regulated in homeostatic way (Karlin 1993; Zoroddu et al. 2019). In cells, Cu ions are coordinated to proteins to be transported, absorbed, or exert their usual catalytic functions. Importantly, in synthetic compounds Cu(I) and Cu(II) can also be coordinated to organic or inorganic groups with different geometries, becoming attractive for medicinal purposes (Linder 1991; Sagripanti et al. 1997a; Haas and Franz 2009; Alvarez et al. 2018).

N-heterocyclic carbene (NHC) complexes are a particular class of interest due to their biological activity against different pathogens as well as human cancer cell lines (de Frémont et al. 2009; Hussaini et al. 2019). Their stability, steric effects and structural diversity are attractive to organometallic chemistry with transition metals (Hussaini et al. 2019; Mariconda et al. 2022), especially for drug design. Among the diverse NHC molecules, silver-based NHCs (Ag-NHCs) have shown activity against bacterial species such as *Salmonella Typhimurium, Listeria monocytogenes,* and *Micrococcus luteus* (Hussaini et al. 2019; Mariconda et al. 2022), and the virus Influenza A/Puerto Rico/8/34 H1N1 (PR8) virus. Similarly, gold-based NHCs (Au-NHCs) have demonstrated activity against the same influenza virus and the *Plasmodium falciparum* parasite (Hussaini et al. 2019; Mariconda et al. 2022).

Recently, our group has reported the biological properties of organometallic Cu(I)-N-heterocyclic carbenes (Cu(I)(NHC)), which are Cu(I) based compounds with a linear geometry, stabilized by the binding of the NHC bearing different N-groups (Fontes et al. 2022). In this context, we can highlight Cu(I)(NHC) based on the symmetric 2,6-diisopropylphenylimidazol-2-ylidene (IPr) and dimesytilimidazol-2-ylidene (IMes). Both were formulated as neutral heteroleptic [Cu(I)(NHC)Cl] and the last one (IMes) was also formulated as the cationic bis-carbene $[Cu(I)(IMes)_2]BF_4$ (**Figure 1**). In addition to previously known anti-leishmanicidal activity, these compounds also presented noteworthy anti-*Chikungunya virus* (CHIKV) activity being the first Cu-NHC complexes effective against RNA viruses (Fontes et al. 2022). Interestingly, the NHCs possess low toxicity in biological systems and are easily modulated to achieve drug-like properties, such as lipophilicity, water stability, and reactivity (Teyssot et al. 2009; Fontes et al. 2022; Al Nasr et al. 2023).

Considering the data described previously and the potential of these metal complexes to be used as a broad-spectrum antiviral, here we evaluated the effects of

Cu(IPr)Cl, Cu(IMes)Cl, and $[Cu(IMes)_2]BF_4$ on the SARS-CoV-2 replication cycle. Further, the effect against Delta and Omicron VoC were characterized and their possible mode of action was suggested.

## 2. METHODS

### 2.1. Cell culture and compounds

Human A549 adenocarcinomic alveolar basal epithelial cells expressing the receptors ACE2 and TRPMSS2 (A549-AT, National Institute for Biological Standards and Control – NIBSC, UK, #101004) and Vero African green monkey kidney cells expressing ACE2 (VERO-E6-ACE2, NIBSC, UK, #101001) were cultivated as previous described (dos Santos Oliveira et al. 2023), using Dulbecco's modified Eagle's medium (DMEM; Sigma–Aldrich, UK) supplemented with 100 U/mL penicillin (Gibco Life Technologies, Thermo-Fisher, UK), 100 mg/mL streptomycin (Gibco Life Technologies), 1% (v/v) non-essential amino acids (Gibco Life Technologies, Thermo-Fisher, UK) and 10% (v/v) fetal bovine serum (FBS; Hyclone, Logan, UT, USA) at 37 °C in a humidified 5% $CO_2$ incubator. The cells were cultivated in the presence of geneticin (G418, Invitrogen, UK) and Hygromycin B (Sigma-Aldrich, UK) at 1 mg/mL and 200 μg/mL, respectively.

The compounds Cu(IPr)Cl, Cu(IMes)Cl, and $[Cu(IMes)_2]BF_4$ were synthesized as previously described (Fontes et al. 2022) and their structures are presented in **Figure 1**. All the compounds were dissolved in DMSO and stored in -20°C for maximum of two days. Dilutions in cell culture media were made immediately prior the assays to achieve DMSO 0.1% (v/v). Molnupiravir (β-D-*N*4-hydroxycytidine) was purchased from Sigma-Aldrich (EIDD-1931, SML2872-5MG), and used at 10 μM as the positive control since it is widely described as coronavirus inhibitor (Teli et al., 2023).

### 2.2. Wild-type SARS-CoV-2 variants

All work with infectious viruses were conducted in biosafety level 3 laboratories at the University of Leeds. The viruses used in this study were obtained and characterized by The Francis Crick Institute The variants include B.1.617.2 - Delta (MS066352H – GISAID accession number EPI_ISL_1731019) and BA.2 – Omicron (hCoV/England/FCI-179/2022, (Shawe-Taylor et al. 2024)). To amplify these viruses, Vero E6-ACE2 cells cultured in 175 $cm^2$ flasks were infected with each variant and

incubated until approximately 80% cytopathic effect was observed. At this time point, cell culture supernatant was collected, and the infectious titre was determined using the 50% tissue culture infectious dose ($TCID_{50}$) method. The calculation of the titre was performed using the Spearman & Kärber algorithm, as outlined (Killington and Hierholzer 1996).

### 2.3. Rescue of recombinant SARS-CoV-2 harboring mNeonGreen marker

The rescue of the SARS-CoV-2 reporter virus (SARS-CoV-2-mNeongreen), based on the NCBI sequence NC_045512.2, was conducted following a previously established protocol (dos Santos Oliveira et al. 2023). Briefly, a total of 1µg pCCI-4K-SARS-CoV-2-mNeonGreen plasmid, containing infectious cDNA under the control of the CMV promoter (Rihn et al. 2021) was transfected into BHK-21 cells ($3x10^5$ cells/well in a 6-well plate) using Lipofectamine 2000 (Thermo-Fisher Scientific, UK) following the manufacturers protocol. After 3 days post transfection the cell culture supernatant was collected and subsequently transferred to A549-AT cells cultured in a 75 $cm^2$ flask until complete cell lysis occurred at which point the supernatant was harvested. The infectious titre of recombinant virus was determined as described above.

### 2.4. Dose-response assay

To assess the impact of Cu(IPr)Cl, Cu(IMes)Cl, and $[Cu(IMes)_2]BF_4$ on both cell viability and viral replication, A549-AT cells were plated at a density of $1x10^4$ cells/well in 96-well plates 24 hours prior to the viral infection. Subsequently, the cells were subjected to treatment with each compound in concentrations ranging from 0.58 to 300µM, employing a two-fold serial dilution scheme. This treatment was conducted in the presence or absence of SARS-CoV-2-mNeonGreen, with a multiplicity of infection (MOI) of 0.1 (Rihn et al. 2021). Cell viability was analysed after 24h by removing the compound-containing media from cells and adding MTT solution at 1mg/mL to each well. After 30 minutes incubation, media was removed and replaced with 100µL of DMSO to solubilize the formazan crystals. The absorbance was measured at 570nm on FLUOstar OPTIMA microplate reader (BMGLabTech). Viral inhibition was analysed after 24h by placing the plates in the IncuCyte® S3 Live-Cell Analysis System (Sartorius) and the green fluorescence signal was recorded at 10x objective. The photos were analysed employing the basic analyser from the IncuCyte S3 system and the total integrated intensity of the fluorescence (GCU x $\mu m^2$/well) was collected. Cell viability and viral replication were calculated according to the equation (T/C) × 100%, which T

and C represented the optical density of the treated/integrated intensity of fluorescence of compound treated wells and control groups, respectively. DMSO was used as vehicle control. The effective concentration of 50% ($EC_{50}$) and cytotoxic concentration of 50% ($CC_{50}$) were calculate as described in the statistical analysis section. The selectivity index (SI) was calculated by dividing the $CC_{50}$ value by the $EC_{50}$ ($SI = CC_{50} / EC_{50}$).

### 2.5. Time of addition assays

For all time of drug addition assays, A549-AT cells at the density of $1\times10^4$ cells per well were seeded in 96 well plates 24h before infection, treatment was performed with Cu(IPr)Cl (10 μM), Cu(IMes)Cl (2 μM), or $[Cu(IMes)_2]BF_4$ (2 μM), and virus replication was assessed by the green fluorescence signal in 10x objective. The photos were analysed employing the basic analyser from the IncuCyte S3 system by the collection of total integrated intensity of the fluorescence (GCU x $\mu m^2$/well). For all assays, DMSO 0.1% (v/v) was used as negative control and Molnupiravir at 10 μM was used a positive control.

In pretreatment assay, cells were initially treated for 1h with each compound, then washed 3x with PBS and added of SARS-CoV-2-mNeonGreen (MOI of 0.1). After 1 h, cells were again washed with PBS, and fresh medium was added for a 24-hour incubation period.

In entry inhibition assay, cells were infected with a combination of each compound and the virus (MOI of 1) for a 1h, washed 3x with PBS, and incubated with fresh medium for 24h. To assess virucidal activity, a similar setup was employed, with the exception that the inoculum, containing both the compound and the virus (amount corresponding to MOI of 5), was incubated for 1h before the introduction to the cells.

Alternatively, the impact of each compound on the attachment step was investigated using the same conditions as the entry inhibition assay, except that the cells were infected with the virus (MOI of 1) in the presence of the compound at a temperature of 4°C. A variation of this assay involved an initial incubation at 4°C, followed by a subsequent 30-minute incubation at 37°C to examine the compound's effect on virus internalization.

In the post-entry assay, cells were infected with SARS-CoV-2-mNeonGreen (MOI of 1) for 1h. Subsequently, the cells underwent washing 3x with PBS and were then incubated in a compound-containing media for 24h. Additionally, a variation of this assay was performed by infecting cells with SARS-CoV-2-mNeonGreen (MOI of 1) for 6 h, followed by incubation with the compound for the remaining duration of the experiment,

allowing the assessment of the compound's effect after the establishment of viral replication.

### 2.6. Measuring activity against SARS-CoV-2 VoCs

To assess the effect of the metal compounds against the delta and omicron variants, the SARS-CoV-2 infectious clone based on Wuhan strain carrying the mCherry reporter gene **(Figure 6A-1)** was modified by replacing the spike gene derivative from the variants B.1.617.2 (delta) or BA.2 (omicron) (**Figure 6A, 2 and 3**). The rescue of the virus was conducted as described above. In the antiviral assay, screening were performed with media containing Cu(IPr)Cl (10 μM), Cu(IMes)Cl (2 μM) and $[Cu(IMes)_2]BF_4$ (2 μM), in the presence of the chimeric Wuhan-B.1.617.2-Spike or Wuhan-BA.2-Spike viruses at a MOI of 0.1. These compound-virus solutions were then added to the cells and incubated for 24 h. Subsequently, the total integrated intensity of fluorescence (measured in RCU x $\mu m^2$ per well) was assessed using the IncuCyte S3 microscope.

For the antiviral assays involving the wild-type VoCs, B.1.617.2 - delta (MS066352H) and BA.2 - omicron (hCoV/England/FCI-179/2022), A549-AT cells were seeded at a concentration of $8x10^5$ cells/well in 12-well plates. These cells were then infected with each virus at an MOI of 0.1 in the presence of Cu(IPr)Cl (10 μM), Cu(IMes)Cl (2 μM), and $[Cu(IMes)_2]BF_4$ (2 μM) for an incubation of 24 h. Following incubation, the supernatant was collected, and the infectious titre was determined using the $TCID_{50}$ method. For all assays, DMSO 0.1% (v/v) was used as negative control and Molnupiravir at 10 μM was used a positive control.

### 2.7. Cell to cell spread assay

To evaluate the effect of the compound in focus formation and cell to cell spread, $5x10^4$ cells were plated in each well of 48 well plates for 24h. Then, cells were infected with SARS-CoV-2-mNeonGreen at an MOI of 0.05 for 1 h, washed with PBS and added of media containing methylcellulose 0.8% and the Cu(IPr)Cl (10 μM), Cu(IMes)Cl (2 μM), or $[Cu(IMes)_2]BF_4$ (2 μM). After 48h, the wells were photographed using the IncuCyte S3 microscope and the quantity of green foci and their size were analysed in each image using ImageJ software and GraphPad Prism 9.

### 2.8. Effect on SARS-CoV-2 proteases $PL^{PRO}$ and $M^{PRO}$

To obtain both pure proteins, $M^{pro}$ (coding region residues 3264-3569) and $PL^{pro}$ (coding region residues 1564-1879), the methodologies of cloning, expression, and purification were conducted as previously described (Fernandes et al. 2021; Freire et al. 2022). Enzymatic inhibition assays were conducted using peptide-based substrates employing FRET (Fluorescence Resonance Energy Transfer). Specific substrates and experimental conditions for each protein were used as described elsewhere (Freire et al. 2022; Noske et al. 2023). In an initial assessment, inhibitor candidates were diluted in DMSO and added to the reaction at a final concentration of 100 μM. Enzymatic activity was monitored by fluorescence using the SpectraMax Gemini EM microplate reader (λ excitation/λ emission 320/420 nm for $PL^{pro}$, and 360/460 nm for $M^{pro}$) at 30s intervals over 30 min. Relative activity was determined by comparison with a control reaction containing an equivalent concentration of DMSO. The inhibition concentration of 50% ($IC_{50}$) values were determined by generating concentration-response curves ranging from 0.98 to 500 μM for each compound, employing a serial dilution factor 2. Curve inflection points and $IC_{50}$ values were determined using the nonlinear regression model [Inhibitor] vs. Response (three parameters) with GraphPad Prism 8 software. Background fluorescence was subtracted using reaction controls devoid of protein. The determined $IC_{50}$ values represent the mean value of three independent experiments.

### 2.9. Molecular docking

Cu(IMes)Cl, Cu(IPr)Cl and $[Cu(IMes)_2]^+$ structures were optimized by DFT, using the ORCA software version 5.0.1 (NEESE, 2012), employing the PBE0 functional (Ernzerhof and Scuseria 1999), def2-TZVP basis function (Weigend and Ahlrichs 2005), def2/J auxiliary basis, RIJCOSX approximation (KOSSMANN; NEESE, 2010), CPCM for implicit DMSO solvation (Tomasi et al. 2005), and a convergence criterion of 1.0 . 10-8 a.u. Minimal verification of the geometry optimizations was made via frequency calculations performed at the same level of theory.

The interaction of these complexes was studied via molecular docking of their optimized structures against the structures of the papain-like ($PL^{pro}$, PDB: 7JIW) (OSIPIUK et al., 2021) and main ($M^{pro}$, PDB: 6LU7) SARS-CoV-2 protease enzymes (Jin et al. 2020). Discovery Studio Visualizer was also utilized for analysing the proteases.

The GOLD software was employed for the docking calculations, utilizing the genetic algorithm (GA) and the ChemPL scoring function. 10 GA runs were carried for

each ligand. The docking binding sites for both enzymes were determined according to the position of the co-crystallized ligands in their respective structures: PLP_Snyder530 for $PL^{pro}$ and N3 for $M^{pro}$, with exact coordinates x: 51.120186, y: 31.882481, z: -0.302333 for $PL^{pro}$, and x: -10.79204, y: 12.417653, z: 68.8122 for $M^{pro}$. The search window was adjusted to 2.857 x Rg8 (the radius of gyration of the complexes, calculated using VMD software), resulting in approximately 20 Å for both.

### 2.10. Statistical analysis

Antiviral assays were performed a minimum of three technical repeats in quadruplicate to confirm the reproducibility of the results. Differences between means of readings were compared using analysis of variance (One-way ANOVA) for the following assays: time of drug addition, wild-type variants, cell-cell spread. *p* values of $<0.05$ (indicated by asterisks) were considered statistically significant. For the establishment of $EC_{50}$ and $CC_{50}$ values, the data were transformed into Log(X), where X is the concentration, and submitted into a non-linear regression log(inhibitor) vs. response with four parameters in variable slope. All analyses were performed using GraphPad Prism 9.

## 3. RESULTS

### 3.1. Cu(NHC) complexes selectively inhibits SAR-CoV-2 replication in A549-AT

To investigate the anti-SARS-CoV-2 activity of Cu(IPr)Cl, Cu(IMes)Cl, and $[Cu(IMes)_2]BF_4$ compounds, A549-AT cells were infected with SARS-CoV-2-mNeongreen and treated with each metal complex in a two-fold serial dilution. As a result, Cu(IPr)Cl had an $CC_{50}$ and $EC_{50}$ of 60.68 ± 3.95 μM and 5.40 ± 2.20 μM, respectively, while Cu(IMes)Cl had an $CC_{50}$ and $EC_{50}$ of 12.26 ± 5.75 μM and 1.13 ± 0.08 μM respectively **(Figure 2A, 2B and 2D)**. For $[Cu(IMes)_2]BF_4$ the $CC_{50}$ and $EC_{50}$ were 6.48 ± 0.56 μM and 1.09 ± 0.11 μM **(Figure 2C and 2D)**. The calculated SI for Cu(IPr)Cl, Cu(IMes)Cl, and $[Cu(IMes)_2]BF_4$ were 11.23, 10.84, and 5.94, respectively **(Figure 2D)**.

### 3.2. Pre-treatment with Cu(IMes)Cl and $[Cu(IMes)_2]BF_4$ protects A549-AT cells against SARS-CoV-2 infection

To elucidate the effect of the complexes on the SARS-CoV-2 replicative cycle, a time of addition assay was performed employing Cu(IPr)Cl at 10 μM, while Cu(IMes)Cl and $[Cu(IMes)_2]BF_4$ were used at 2 μM. First the cells were pre-treated for 1 h with each complex, followed by PBS washing and infection with the SARS-CoV-2-mNeonGreen (MOI of 0.1) for additional 1h **(Figure 3A)**. Then cells were washed 3x with PBS to

remove unbound virus and fresh media was added to the cells. The results showed that Cu(IMes)Cl and $[Cu(IMes)_2]BF_4$ pretreatment decreased SARS-CoV-2-mNeonGreen infection by 99.9% and 87.7% ($p<0.0001$) respectively **(Figure 3B)**. However, Cu(IPr)Cl did not show any protection effect **(Figure 3B)**. Molnupiravir, the positive control, on the other hand, inhibited 25% of SARS-CoV-2 replication in the same assay.

### 3.3. Cu(I)(NHC) complexes impair several stages of SARS-CoV-2 entry to the host cell

To evaluate the effects of Cu(I)(NHC) on SARS-CoV-2-mNeonGreen entry, virus (MOI of 1) and each complex were simultaneously added to A549-AT cells for 1 h at 37°C, and inoculum was replaced with fresh media **(Figure 4A)**. Cu(IPr)Cl inhibited virus entry by 48.1%, while Cu(IMes)Cl and $[Cu(IMes)_2]BF_4$ had a more prominent effect: 99.6% and 74% ($p < 0.0001$) inhibition was observed, respectively **(Figure 4B)**. A modification of this protocol by including 1 h pre-incubation of the inoculum containing each complex and virus (MOI of 5) at 37 °C, prior to the infection and treatment of the cells **(Figure 4C)**, decreased fluorescence intensity by 58.5%, 100%, and 90.7% for Cu(IPr)Cl, Cu(IMes)Cl, and $[Cu(IMes)_2]BF_4$, ($p < 0.0001$) respectively, indicating that these complexes also possess virucidal activity **(Figure 4D)**.

To analyse the effect of Cu(IPr)Cl, Cu(IMes)Cl, and $[Cu(IMes)_2]BF_4$ on SARS-CoV-2 attachment, virus (MOI of 1) and complexes were first incubated with the cells at 4 °C for 1 h. At this temperature, virus particles were able to attach to the cellular receptors, but not enter the host cells. Cells were then washed with PBS, fresh media was added, and cultures incubated at 37 °C for 24h **(Figure 4E)**. Data obtained from this assay also showed strong inhibition of SARS-CoV-2-mNeonGreen attachment by Cu(IPr)Cl, Cu(Imes)Cl, and $[Cu(Imes)_2]BF_4$, reducing virus entry by 67%, 99.4%, and 72.5% respectively ($p < 0.0001$) **(Figure 4F)**. Further, post-attachment was evaluated by including an additional incubation of 30 min at 37°C to the previous protocol **(Figure 4G).** The additional inhibition step had no prominent effect on virus inhibition which was 53.3%, 99.9%, and 79.2%, for Cu(IPr)Cl, Cu(IMes)Cl and $[Cu(IMes)_2]BF_4$, respectively ($p < 0.0001$) **(Figure 4H)**. In all entry assays evaluated, Molnupiravir inhibit SARS-CoV-2 fluorescence in entry, attachment, and post-attachment around ≤ 50%, while was not active in virucidal assay (**Figure 4A-H)**.

### 3.4. Cu(IPr)Cl, Cu(IMes)Cl, and $[Cu(IMes)_2]BF_4$ potently impair post-entry stages of SARS-CoV-2 replication

To assess the effect of the complexes on post-entry steps of SARS-CoV-2 infection, the cells were infected with SARS-CoV-2-mNeonGreen (MOI of 1) for 1 h, or 6 h, and fresh media containing each complex was added **(Figure 5A and 5B)**. Analysis performed after 24h, revealed that all complexes inhibited the viral replication in over 98% when added after 1h infection ($p < 0.0001$) **(Figure 5A and 5C**). Interestingly, when added 6h after viral infection **(Figure 5B)**, the complexes were still able to suppress SARS-CoV-2-mNeonGreen replication, Cu(IPr)Cl, Cu(IMes)Cl, and $[Cu(IMes)_2]BF_4$ decreased fluorescence by 95%, 99.9%, and 87.6%, respectively ($p < 0.0001$) **(Figure 5D)**. Molnupiravir strongest effect was also observed in post-entry assays, inhibiting more that 95% of SARS-CoV-2 replication (**Figure 5B and 5D**).

### 3.5. Cu(I)(NHC) complexes possess a broad-spectrum activity against Delta (B.1.17.2) and Omicron (BA.2) variants

As Cu(IPr)Cl, Cu(IMes)Cl, and $[Cu(IMes)_2]BF_4$ potently inhibited infection of the Wuhan strain of SARS-CoV-2 we also evaluated their impact on the two recent VoCs, B.1.617.2 (delta) and BA.2 (omicron). First the assay was performed using chimeras where the spike (S) protein region of the Wuhan strain infectious clone was replaced by its counterpart from Delta or Omicron; all clones also contained the mCherry reporter **(Figure 6A)**. Infectious viruses were rescued and used to infect A539-AT cells in the presence or absence of Cu(IPr)Cl (10 μM), Cu(IMes)Cl (2 μM), and $[Cu(IMes)_2]BF_4$ (2 μM) for 24h. The results show that Cu(IPr)Cl, Cu(IMes)Cl, and $[Cu(IMes)_2]BF_4$ decreased viral replication by 61%, 94.6%, and 92.1% ($p < 0.0001$), respectively, when assayed against the SARS-CoV-2 Wuhan-B.1.617.2-Spike **(Figure 6B)**. Similarly, against SARS-CoV-2 Wuhan-BA.2-Spike these complexes inhibited 69.8%, 99.7%, and 97.3% ($p < 0.0001$) respectively **(Figure 6C)**. Similarly, Molnupiravir was able to decrease both chimera variants in more than 98% (**Figure 6B and 6C**).

Moreover, we evaluated the effect of Cu(IPr)Cl, Cu(IMes)Cl, and $[Cu(IMes)_2]BF_4$ against the patient-derivative variants B.1.617.2 (Delta) or BA.2 (Omicron). Reassuringly, when the complexes were added to cells in the presence of each variant, the inhibitory profile of those viruses was similar to that observed using recombinant viruses. Against the B.1.617.2 (Delta) variant, Cu(IPr)Cl decreased the viral titre by 0.5 $Log_{10}$, but with no statistical significance, while Cu(IMes)Cl and $[Cu(IMes)_2]BF_4$ significantly decreased titres by 3 $Log_{10}$ ($p < 0.001$) and 1 $Log_{10}$ ($p < 0.01$), respectively

**(Figure 7A)**. In contrast, all compounds when evaluated against the BA.2 (Omicron) demonstrated significant effect on viral titres: 1.2 $Log_{10}$, 2.1 $Log_{10}$, and 2 $Log_{10}$ for Cu(IPr)Cl, Cu(IMes)Cl, and $[Cu(IMes)_2]BF_4$, respectively **(Figure 7B)**. Interestingly, Molnupiravir decreased viral titre in 4 $Log_{10}$ in comparison to the control in against both Delta and Omicron wild-type variants **(Figure 7A and 7B)**.

### 3.6. Cu(IMes)Cl and $[Cu(IMes)_2]BF_4$ inhibit SARS-CoV-2 proteases at low concentrations

The copper(II) complexes containing tridentate Schiff Base ligands were found to be an inhibitor of papain-like protease ($PL^{pro}$) activity in SARS-CoV replication as well as binding to coronaviruses main protease ($M^{pro}$) (ALBALAWI et al., 2024; GARZA-LOPEZ; KOZAK; GRAY, 2020). As the strongest effect of our Cu(I)(NHC) compounds on post-entry stages of SARS-CoV-2 replication implies that these compounds may target viral enzymes, we analysed activities of these compounds against the $PL^{pro}$ and $M^{pro}$. It was observed that Cu(IMes)Cl complex inhibit the protease activity of $PL^{pro}$ with a half maximal inhibitory concentration ($IC_{50}$) of 6.1 μM (**Figure 8A**). At concentrations ≥ 25 μM Cu(IMes)Cl also inhibited activity of $M^{pro}$ but the degree of inhibition was modest: even at the highest concentration (200 μM) approximately 35% inhibition was observed **(Figure 8B**). These findings suggest that Cu(IMes)Cl main target is the $PL^{pro}$, even though, it might also impair $M^{pro}$ protease activity in nonspecific effect. On the other hand, $[Cu(IMes)_2]BF_4$ only inhibited $M^{pro}$: up to 60% of inhibition of protease activity was observed at concentrations ≥ 30 μM (**Figure 8B**), but did not inhibit $PL^{pro}$ activity. In contrast, Cu(IPr)Cl did not inhibit any of the proteases evaluated.

Next, the Cu(I)(NHC) compounds were docked into the structures of $PL^{pro}$ (PDB 7JIW) and $M^{pro}$ (PDB 6LU7), both of which were co-crystallized with inhibitors Snyder530 and N3 respectively (JIN et al., 2020; OSIPIUK et al., 2021). Snyder530 is a non-covalent inhibitor of $PL^{pro}$, whereas N3 acts as a Michael acceptor inhibitor of $M^{pro}$ by forming a covalent bond with Cys145. Subsequently, the structures were processed to remove inhibitors and salts, including the zinc ion from the zinc-binding domain of $PL^{pro}$. The regions where the co-crystallized inhibitors interact with the active site were utilized as a guide for docking the Cu(I)(NHC) compounds.

Analysis of the charge distribution in both $PL^{pro}$ and $M^{pro}$ revealed predominantly neutral surfaces **(Figure S1)** in both proteins. The CHEMPLP Fitness scores for the highest-scoring poses of each complex **(Table 1)** appear to partially mirror the

experimental results obtained. Specifically, the most potent compound against $PL^{pro}$, Cu(IMes)Cl, exhibited the highest score (55.5123) **(Figure 8B)**, followed by $[Cu(IMes)_2]BF_4$ (54.9629) and Cu(IPr)Cl (53.9465) **(Table 1)**. Similarly, for $M^{pro}$, $[Cu(IMes)_2]BF_4$, hereafter named as $[Cu(IMes)_2]^+$ achieved the highest score (61.9902), which notably surpassed the other compounds (52.2707; 50.1214) and correlates well with experimental findings **(Figure 8D and Table 1)**.

The active site of $PL^{pro}$ predominantly comprises hydrophobic residues, with the catalytic triad (Cys111-His272-Asp286) located at the terminal portion. Similar to Snyder530, Cu(I)(NHC) compounds can engage in comparable hydrophobic interactions with Pro248, Tyr264, and Tyr268. Notably, the planarity and reduced bulkiness of Cu(IMes)Cl appear to facilitate better accommodation for non-covalent interactions with the hydrophobic region compared to other compounds that are more sterically demanding (**Figure 8C, Figure S2-3**). In the case of $M^{pro}$, Cu(I)(NHC) compounds interact non-covalently with the catalytic dyad present in $M^{pro}$, particularly with residues His41, Met49, Cys145, His154, and Met165 (**Figure 8D and Table 1, Figure S2-3**).

While we speculate that the most effective Cu(I)(NHC) inhibitors may engage in covalent binding after non-covalent recognition of the active site, such predictions are not within the scope of docking analysis. Nonetheless, non-covalent interactions could still play a crucial role in ligand recognition and interaction, as highlighted in this study. Notably, the bulkier $[Cu(IMes)_2]BF_4$ compound may efficiently interact with $M^{pro}$, potentially hindering subsequent covalent binding due to steric hindrance, suggesting the reason for the experimental observation.

**Table 1. CHEMPLP Fitness score, and Interacting residues for the best poses obtained in the Docking calculations for Cu(IMes)Cl, Cu(IPr)Cl and $[Cu(IMes)_2]^+$.**

| **$PL^{pro}$** | | |
|---|---|---|
| Compound | CHEMPLP Score | Interacting residues |
| Cu(IMes)Cl | 55.5123 | Arg166, Tyr247, Pro248, Tyr264, Tyr268 |
| Cu(IPr)Cl | 53.9465 | Asp164, Ala246, Pro248, Tyr264, Tyr268 |
| $[Cu(IMes)_2]^+$ | 54.9629 | Arg166, Pro248, Tyr264, Tyr268 |

| $M^{pro}$ | | |
|---|---|---|
| Compound | CHEMPLP Score | Interacting residues |
| Cu(IMes)Cl | 52.2707 | His41, Met49, Cys145, His164, Met165 |
| Cu(IPr)Cl | 50.1214 | Met49, Cys145, His164, Glu166 |
| $[Cu(IMes)_2]^+$ | 61.9902 | His41, Met49, His164, Met165 |

### 3.7. $[Cu(IMes)_2]BF_4$ impairs SARS-CoV-2 cell to cell transmission *in vitro*

Cell-to-cell transmission has been described as an important feature of SARS-CoV-2 spread and pathogenesis, and compounds that can inhibit this transmission are widely required (Zeng et al. 2022). Here we evaluated SARS-CoV-2 cell to cell spread by measuring the size of fluorescence foci in the presence of each compound, employing SARS-CoV-2-mNeonGreen. In this experiment, A549-AT cells were infected with virus at an MOI of 0.05 for 1h and then treated with each complex in the presence of methylcellulose 0.8%. After treatment, only $[Cu(IMes)_2]BF_4$ decreased size focus of infected cells in 0.08 μm² (control 0.30 μm², while $[Cu(IMes)_2]BF_4$ treated 0.22 μm²) **(Figure 9A and 9B)**.

## 4. DISCUSSION

The biological effects of Cu(IPr)Cl, Cu(IMes)Cl, and $[Cu(IMes)_2]BF_4$ especially their antiviral activity against CHIKV were previously described by our group and they presented potent inhibition of CHIKV at 2 μM. Nevertheless, no assessment of anti-SARS-CoV-2 activity and mainly the potential mechanisms of antiviral effects were conducted (Fontes et al. 2022). In this context, through different assays we identified here different cytotoxic and antiviral profile among these complexes. The Cu(IPr)Cl, Cu(IMes)Cl, and $[Cu(IMes)_2]BF_4$ had selectivity indexes (SI) of 11.23, 10.84, and 5.94, respectively. The difference in SIs among these metallodrugs might be explained by the their lipophilicity (Berthod and Carda-Broch 2004; Giaginis et al. 2018; Fontes et al. 2022), being the least lipophilic to the most lipophilic, Cu(IPr)Cl, followed by Cu(IMes)Cl, and $[Cu(IMes)_2]BF_4$, in this order (Fontes et al. 2022). In this case, for

Cu(IPr)Cl the lower lipophilicity and higher stability in solution can be the reason for lower cytotoxicity. This might be due to the lower cell uptake in comparison to compounds with higher lipophilicity (Giaginis et al. 2018; Fontes et al. 2022). Alternatively, $[Cu(IMes)_2]BF_4$ high lipophilicity resulted in more active molecule (lowest $EC_{50}$), but less selective due to the higher cytotoxicity to cells. Additionally, $[Cu(IMes)_2]BF_4$ had a high cytotoxicity in BHK-21 cells and RAW macrophages, agreeing with the results described here (Fontes et al. 2022). What is more interesting, Cu(IMes)Cl was known to go under chemical speciation in solution, forming [Cu(IMes)] in an chemical equilibrium (Berthod and Carda-Broch 2004; Meanwell 2018; Fontes et al. 2022). The study on $[Cu(IMes)_2]BF_4$ confirmed the potent cytotoxic effects of the $[Cu(IMes)_2]^+$ cation, which also exhibits the lowest $EC_{50}$ against SARS-CoV-2. This strongly suggests that the cation plays a key role in the overall biological activity of Cu(IMes)Cl. To assess the contribution of the anionic species $CuCl_2^-$, we attempted to test commercial CuCl (cuprous chloride). However, the compound proved unstable in aqueous solution, rapidly oxidizing to $Cu^{2+}$ upon dissolution. But the results suggest that these Cu(NHC) complexes possess a close relationship among structure-activity. This fact is also reinforced by the remarkable activity on B.1.617.2 (delta) and (omicron) variants, which probably are not related to the S glycoprotein, since the insertion of them in the Wuhan strain infectious clone did not cause any decrease in inhibition.

Furthermore, the metallodrug Cu(IPr)Cl did not protect the cells against SARS-CoV-2 infection, but impaired SARS-CoV-2 entry (all steps over 65%), as well as its replication. Differently, both Cu(IMes)Cl and $[Cu(IMes)_2]BF_4$ were able to strongly impair all viral stages evaluated here, with an overall inhibition of over 70%, reaching the complete knockdown of virus infection (100% inhibition) for some protocols, specially under the treatment with Cu(IMes)Cl. The Cu ions are reactive oxygen species (ROS) inducing molecules in mammalian cells (Novello and Stirpe 1969; Sagripanti et al. 1993, 1997a; Shionoiri et al. 2012; Erxleben 2018), and since other Cu(II) complexes where characterized as capable of speciation in biological systems, probably releasing the Cu(II) ions (dos Santos Oliveira et al. 2023), it is possible to hypothesize that the chemical speciation might also be related to their activity on viral replication cycle. The presence of ROS in infected cells could play important role in impairing RNA replication and viral assemble and maturation, which are essential to generate new virions (Sagripanti et al. 1997b; Boas and Reches 2021; Sander et al. 2022; Jadaun et al. 2023). The decreased capacity of chemical speciation of Cu(IPr)Cl, with more stable molecule does not provide

enough Cu(I) ions, that can result in ROS and/or other immune pathway activation, therefore agrees with the lack of protective activity (Creaven et al. 2010; Schieber and Chandel 2014; Cavicchioli et al. 2019). In contrast, both Cu(IMes)Cl and $[Cu(IMes)_2]BF_4$ might produce copper ions in biological milieu, resulting in a strong protective activity through that mechanism. Furthermore, the potent entry inhibition of Cu(I)(NHC) might also be related to the chemical speciation, since the coordination with Cu can result in molecules that can disrupt the viral envelope (Sagripanti et al. 1993, 1997a; Grass et al. 2011).

The post-entry effect of all Cu(I)(NHC) also needs to be highlighted since they were able to recover inhibition after SARS-CoV-2 replication complex was stablished (Klein et al. 2020; V'kovski et al. 2021). Recently, silver coordinated to N-heterocyclic carbenes (Ag(I)-NHC) were described as SARS-CoV-2 inhibitors with SI ranging between 3 to 100, and with a direct interaction with the SARS-CoV-2 $PL^{pro}$ (Gil-Moles et al. 2023). Firstly, it is important to emphasize that the SARS-CoV-2 infection was performed in an MOI 10-fold higher than the one used here on our dose response assay (Gil-Moles et al. 2023). However, their data still supports the Ag(I)(NHC) strong effect on viral post-entry, probably by impairing viral RNA replication.

Besides, our results suggest a multitarget nature of the compounds, where $[Cu(IMes)_2]BF_4$ might be inhibiting SARS-CoV-2 replication by interacting with $M^{pro}$, but no other activity of this compound can be discarded. On the other hand, Cu(IPr)Cl did not inhibit $M^{pro}$ or $PL^{pro}$ catalytic activities, therefore its antiviral activity might be on other viral proteins or even in cell metabolism. Notably, Cu(IMes)Cl inhibited $PL^{pro}$ activity at a low micromolar range, thereby suggesting that the viral papain-like protease is a target for this compound and a possible mechanism of action underlying the replication inhibition. Recently, neutral and cationic Au(NHC) that impairs SARS-CoV-2 replication effectively demonstrated to inhibit $PL^{pro}$ in similar range of $IC_{50}$ that Cu(IMes)Cl. The mechanism of a series of Au(NHC) was demonstrated to be not only the binding to the cysteine in the active site, but also eject zinc from a zinc binding domain responsible for correct folding and substrate approach (Gil-Moles et al. 2020). Our research for long has been demonstrating the ability of metal-based compounds to target zinc binding domains impairing the proteins and enzymes activity with some selectivity depending on the coordination sphere (Abbehausen et al. 2018; Aðalsteinsson et al. 2020; Galuppo et al. 2023). The docking analysis demonstrated that Cu(IMes)Cl can non-

covalently interact with hydrophobic residues of catalytic site. Further studies are needed to evaluate covalent binding and or zinc ejection.

## 5. CONCLUSION

The data presented here advocates for the multiple antiviral effects of Cu(I)(NHC) organometallic compounds against SARS-CoV-2 replication *in vitro*. The compounds were effective not only against Wuhan strain, but also the B.1.617.2 and BA.2 variants. $[Cu(IMes)_2]BF_4$ demonstrated its capacity of limiting SARS-CoV-2 cell to cell spread. Cu(IMes)Cl was identified as a potent inhibitor of SARS-CoV-2 $PL^{pro}$ protease activity. Based on these results, we strongly encourage further investigations involving Cu(NHC) compounds, deciphering their specific antiviral effects and potential off-target effect. Furthermore, we propose that Cu(IMes)Cl to be considered for utilization in pre-clinical assays as a promising alternative for the treatment of COVID-19.

### Author contributions: CRediT

**Conceptualization:** Igor Andrade Santos; Camilla Abbehausen; Mark Harris; Ana Carolina Gomes Jardim. **Data curation:** Igor Andrade Santos; Josielle V. Fontes; Gustavo C. Rodrigues; Mariana Ortiz de Godoy. **Formal analysis:** Igor Andrade Santos; Josielle V. Fontes. **Funding acquisition:** Camilla Abbehausen; Mark Harris; Ana Carolina Gomes Jardim. **Investigation:** Igor Andrade Santos; Josielle V. Fontes. **Methodology:** Igor Andrade Santos; Josielle V. Fontes; Gustavo C. Rodrigues, Mariana Ortiz de Godoy, Glaucius Oliva, Rafael V. C. Guido; Andres Merits. **Project administration:** Camilla Abbehausen; Mark Harris; Ana Carolina Gomes Jardim. **Resources and Supervision:** Mark Harris; Ana Carolina Gomes Jardim. **Validation:** Igor Andrade Santos. **Visualization:** Mark Harris; Ana Carolina Gomes Jardim. **Writing – original draft:** Igor Andrade Santos; Josielle V. Fontes; Gustavo C. Rodrigues, Mariana Ortiz de Godoy, Glaucius Oliva, Rafael V. C. Guido; Mark Harris; Ana Carolina Gomes Jardim

### Declaration of competing interest

The authors declare that they have no known competing financial interests or personal relationships that could have appeared to influence the work reported in this paper.


### ACKNOWLEGEMENTS

Work in the MH laboratory was funded by the Medical Research Council (grant numbers MR/S001026/1 and MR/V036904/1). The Incucyte S3 purchase was funded by a Wellcome Multi-User Equipment grant (221538/Z/20/Z). A. C. G. J. is grateful to FAPEMIG (Minas Gerais Research Foundation APQ-01487-22 and APQ-04686-22) and

to CAPES (Prevention and Combat of Outbreaks, Endemics, Epidemics and Pandemics—Finance Code #88881.506794/2020-01 and —Finance Code 001). I. A. S. thanks to Coordenação de Aperfeiçoamento de Pessoal de Nível Superior (CNPq), for scholarship #142495/2020-4, CAPES.PrInt-UFU sandwich scholarship #88887.700246/2022-00, and FAPEMIG postdoctoral scholarship # 67355. CA thanks the financial support from São Paulo Research Foundation (FAPESP) Processes # 2022/02618-0, # 2020/04602-9, and #2013/07600-3 and Brazilian National Council of Research (CNPq) 404668/2021-6. GCR thanks FAPESP for the scholarship 2023/12657-6. JVF thanks FAPESP for the scholarship 2022/06410-5. CA and GCR thanks CENAPAD for the computational support Proj 168.

## REFERENCES

Abbehausen C, de Paiva REF, Bjornsson R, et al (2018) X-ray Absorption Spectroscopy Combined with Time-Dependent Density Functional Theory Elucidates Differential Substitution Pathways of Au(I) and Au(III) with Zinc Fingers. Inorg Chem 57:. https://doi.org/10.1021/acs.inorgchem.7b02406

Aðalsteinsson HM, Lima FA, Galuppo C, Abbehausen C (2020) Evaluation of cobalt complexes with tripod ligands for zinc finger targeting. Dalton Transactions 49:. https://doi.org/10.1039/D0DT00067A

Al Nasr IS, Koko WS, Khan TA, et al (2023) Evaluation of Ruthenium(II) N-Heterocyclic Carbene Complexes as Enzymatic Inhibitory Agents with Antioxidant, Antimicrobial, Antiparasitical and Antiproliferative Activity. Molecules 28:1359. https://doi.org/10.3390/molecules28031359

Alvarez N, Kramer MG, Ellena J, et al (2018) Copper-diimine coordination compounds as potential new tools in the treatment of cancer. Cancer Rep Rev 2:. https://doi.org/10.15761/CRR.1000161

Augustin M, Schommers P, Stecher M, et al (2021) Post-COVID syndrome in non-hospitalised patients with COVID-19: a longitudinal prospective cohort study. The Lancet Regional Health - Europe 6:100122. https://doi.org/10.1016/J.LANEPE.2021.100122

Berthod A, Carda-Broch S (2004) Determination of liquid–liquid partition coefficients by separation methods. J Chromatogr A 1037:3–14. https://doi.org/10.1016/j.chroma.2004.01.001

Boas D, Reches M (2021) A Novel Copper-Binding Peptide That Self-Assembles Into a Transparent Antibacterial and Antiviral Coating. Front Bioeng Biotechnol 9:. https://doi.org/10.3389/fbioe.2021.736679

Boros E, Dyson PJ, Gasser G (2020) Classification of Metal-Based Drugs according to Their Mechanisms of Action. Chem 6:41–60. https://doi.org/10.1016/j.chempr.2019.10.013

Cavicchioli M, Zaballa A, Paula Q, et al (2019) Oxidative Assets Toward Biomolecules and Cytotoxicity of New Oxindolimine-Copper(II) and Zinc(II) Complexes. Inorganics (Basel) 7:12. https://doi.org/10.3390/inorganics7020012

592 Creaven BS, Duff B, Egan DA, et al (2010) Anticancer and antifungal activity of copper(II)
593 complexes of quinolin-2(1H)-one-derived Schiff bases. Inorganica Chim Acta 363:4048–
594 4058. https://doi.org/10.1016/j.ica.2010.08.009

595 de Frémont P, Marion N, Nolan SP (2009) Carbenes: Synthesis, properties, and organometallic
596 chemistry. Coord Chem Rev 253:. https://doi.org/10.1016/j.ccr.2008.05.018

597 de Paiva REF, Marçal Neto A, Santos IA, et al (2020) What is holding back the development of
598 antiviral metallodrugs? A literature overview and implications for SARS-CoV-2
599 therapeutics and future viral outbreaks. Dalton Transactions 49:16004–16033.
600 https://doi.org/10.1039/D0DT02478C

601 dos Santos Oliveira L, de Souza Guarda PH, Rosa LB, et al (2023) Exploring the copper(II)
602 coordination to 2'-hydroxy-4-benzyloxychalcone analogues and their potential
603 pharmacological applications. Inorganica Chim Acta 121806.
604 https://doi.org/10.1016/j.ica.2023.121806

605 Duffy S (2018) Why are RNA virus mutation rates so damn high? PLoS Biol 16:e3000003.
606 https://doi.org/10.1371/journal.pbio.3000003

607 Ernzerhof M, Scuseria GE (1999) Assessment of the Perdew–Burke–Ernzerhof exchange-
608 correlation functional. J Chem Phys 110:. https://doi.org/10.1063/1.478401

609 Erxleben A (2018) Interactions of copper complexes with nucleic acids. Coord Chem Rev
610 360:92–121. https://doi.org/10.1016/j.ccr.2018.01.008

611 Fernandes RS, de Godoy AS, Santos IA, et al (2021) Discovery of an imidazonaphthyridine and
612 a riminophenazine as potent anti-Zika virus agents through a replicon-based high-
613 throughput screening. Virus Res 299:198388.
614 https://doi.org/10.1016/j.virusres.2021.198388

615 Fontes J V., Santos IA, Rosa LB, et al (2022) Antileishmanial and Anti-Chikungunya Activity of
616 Cu(I)-N-Heterocyclic Carbenes. ChemistrySelect 7:.
617 https://doi.org/10.1002/slct.202201560

618 Freire MCLC, Basso LGM, Mendes LFS, et al (2022) Characterization of the RNA-dependent
619 RNA polymerase from Chikungunya virus and discovery of a novel ligand as a potential
620 drug candidate. Sci Rep 12:. https://doi.org/10.1038/s41598-022-14790-x

621 Galuppo C, Gomes de Oliveira Junior A, dos Santos Oliveira L, et al (2023) Reactivity of NiII,
622 PdII and PtII complexes bearing phosphine ligands towards ZnII displacement and
623 hydrolysis in Cis2His2 and Cis3His zinc-fingers domains. J Inorg Biochem 240:.
624 https://doi.org/10.1016/j.jinorgbio.2022.112117

625 Giaginis C, Tsopelas F, Tsantili-Kakoulidou A (2018) The Impact of Lipophilicity in Drug
626 Discovery: Rapid Measurements by Means of Reversed-Phase HPLC. pp 217–228

627 Gil-Moles M, Basu U, Büssing R, et al (2020) Gold Metallodrugs to Target Coronavirus Proteins:
628 Inhibitory Effects on the Spike-ACE2 Interaction and on PLpro Protease Activity by
629 Auranofin and Gold Organometallics**. Chemistry – A European Journal 26:.
630 https://doi.org/10.1002/chem.202004112

631 Gil-Moles M, O'Beirne C, Esarev I V., et al (2023) Silver N-heterocyclic carbene complexes are
632 potent uncompetitive inhibitors of the papain-like protease with antiviral activity against
633 SARS-CoV-2. RSC Med Chem 14:1260–1271. https://doi.org/10.1039/D3MD00067B

Grass G, Rensing C, Solioz M (2011) Metallic Copper as an Antimicrobial Surface. Appl Environ Microbiol 77:1541–1547. https://doi.org/10.1128/AEM.02766-10

Grasselli G, Tonetti T, Protti A, et al (2020) Pathophysiology of COVID-19-associated acute respiratory distress syndrome: a multicentre prospective observational study. Lancet Respir Med 8:1201–1208. https://doi.org/10.1016/S2213-2600(20)30370-2

Haas KL, Franz KJ (2009) Application of Metal Coordination Chemistry To Explore and Manipulate Cell Biology. Chem Rev 109:4921–4960. https://doi.org/10.1021/cr900134a

Hussaini SY, Haque RA, Razali MR (2019) Recent progress in silver(I)-, gold(I)/(III)- and palladium(II)-N-heterocyclic carbene complexes: A review towards biological perspectives. J Organomet Chem 882:. https://doi.org/10.1016/j.jorganchem.2019.01.003

Jadaun P, Shah P, Harshithkumar R, et al (2023) Antiviral and ROS scavenging potential of Carica papaya Linn and Psidium guajava leaves extract against HIV-1 infection. BMC Complement Med Ther 23:. https://doi.org/10.1186/s12906-023-03916-x

Jayk Bernal A, Gomes da Silva MM, Musungaie DB, et al (2022) Molnupiravir for Oral Treatment of Covid-19 in Nonhospitalized Patients. New England Journal of Medicine 386:509–520. https://doi.org/10.1056/NEJMoa2116044

Jin Z, Du X, Xu Y, et al (2020) Structure of Mpro from SARS-CoV-2 and discovery of its inhibitors. Nature 582:. https://doi.org/10.1038/s41586-020-2223-y

Johnson AG, Amin AB, Ali AR, et al (2022) COVID-19 Incidence and Death Rates Among Unvaccinated and Fully Vaccinated Adults with and Without Booster Doses During Periods of Delta and Omicron Variant Emergence — 25 U.S. Jurisdictions, April 4–December 25, 2021. MMWR Morb Mortal Wkly Rep 71:132–138. https://doi.org/10.15585/MMWR.MM7104E2

Karlin KD (1993) Metalloenzymes, Structural Motifs, and Inorganic Models. Science (1979) 261:701–708. https://doi.org/10.1126/science.7688141

Killington, Hierholzer (1996) Virology Methods Manual

Klein S, Cortese M, Winter SL, et al (2020) SARS-CoV-2 structure and replication characterized by in situ cryo-electron tomography. Nat Commun 11:5885. https://doi.org/10.1038/s41467-020-19619-7

Lamers MM, Haagmans BL (2022) SARS-CoV-2 pathogenesis. Nat Rev Microbiol 20:270–284. https://doi.org/10.1038/s41579-022-00713-0

Linder MC (1991) Biochemistry of Copper. Springer US, Boston, MA

Liu J, Pan X, Zhang S, et al (2023) Efficacy and safety of Paxlovid in severe adult patients with SARS-Cov-2 infection: a multicenter randomized controlled study. Lancet Reg Health West Pac 33:100694. https://doi.org/10.1016/j.lanwpc.2023.100694

Maltezou HC, Pavli A, Tsakris A (2021a) Post-COVID Syndrome: An Insight on Its Pathogenesis. Vaccines (Basel) 9:497. https://doi.org/10.3390/vaccines9050497

Maltezou HC, Pavli A, Tsakris A (2021b) Post-COVID Syndrome: An Insight on Its Pathogenesis. Vaccines 2021, Vol 9, Page 497 9:497. https://doi.org/10.3390/VACCINES9050497

Mariconda A, Iacopetta D, Sirignano M, et al (2022) *N* -Heterocyclic Carbene (NHC) Silver Complexes as Versatile Chemotherapeutic Agents Targeting Human Topoisomerases and Actin. ChemMedChem 17:. https://doi.org/10.1002/cmdc.202200345

Messerschmidt A, Huber R, Poulas T, et al (eds) (2004) Handbook of Metalloproteins. Wiley

Montagutelli X, Prot M, Levillayer L, et al (2021) The B1.351 and P.1 variants extend SARS-CoV-2 host range to mice. https://doi.org/10.1101/2021.03.18.436013

Noske GD, de Souza Silva E, de Godoy MO, et al (2023) Structural basis of nirmatrelvir and ensitrelvir activity against naturally occurring polymorphisms of the SARS-CoV-2 main protease. Journal of Biological Chemistry 299:. https://doi.org/10.1016/j.jbc.2023.103004

Novello F, Stirpe F (1969) The effects of copper and other ions on the ribonucleic acid polymerase activity of isolated rat liver nuclei. Biochemical Journal 111:115–119. https://doi.org/10.1042/bj1110115

Oronsky B, Larson C, Hammond TC, et al (2021) A Review of Persistent Post-COVID Syndrome (PPCS). Clin Rev Allergy Immunol 1:1–9. https://doi.org/10.1007/S12016-021-08848-3/TABLES/3

Pantazis N, Pechlivanidou E, Antoniadou A, et al (2023) Remdesivir: Effectiveness and Safety in Hospitalized Patients with COVID-19 (ReEs-COVID-19)—Analysis of Data from Daily Practice. Microorganisms 11:1998. https://doi.org/10.3390/microorganisms11081998

Rihn SJ, Merits A, Bakshi S, et al (2021) A plasmid DNA-launched SARS-CoV-2 reverse genetics system and coronavirus toolkit for COVID-19 research. PLoS Biol 19:e3001091. https://doi.org/10.1371/journal.pbio.3001091

Sagripanti JL, Routson LB, Bonifacino AC, Lytle CD (1997a) Mechanism of copper-mediated inactivation of herpes simplex virus. Antimicrob Agents Chemother 41:812–817. https://doi.org/10.1128/AAC.41.4.812

Sagripanti JL, Routson LB, Bonifacino AC, Lytle CD (1997b) Mechanism of copper-mediated inactivation of herpes simplex virus. Antimicrob Agents Chemother 41:. https://doi.org/10.1128/AAC.41.4.812

Sagripanti JL, Routson LB, Lytle CD (1993) Virus inactivation by copper or iron ions alone and in the presence of peroxide. Appl Environ Microbiol 59:4374–4376. https://doi.org/10.1128/aem.59.12.4374-4376.1993

Sander WJ, Fourie C, Sabiu S, et al (2022) Reactive oxygen species as potential antiviral targets. Rev Med Virol 32:. https://doi.org/10.1002/rmv.2240

Sanderson T, Hisner R, Donovan-Banfield I, et al (2023) A molnupiravir-associated mutational signature in global SARS-CoV-2 genomes. Nature. https://doi.org/10.1038/s41586-023-06649-6

Saúde. M da S de V à S (2022) Anvisa aprova uso emergencial do medicamento Paxlovid para Covid-19. https://www.gov.br/anvisa/pt-br/assuntos/noticias-anvisa/2022/anvisa-aprova-uso-emergencial-do-medicamento-paxlovid-para-covid-19#:~:text=A Diretoria Colegiada (Dicol) da,Pública da Dicol de 2022. Accessed 1 May 2022

Schieber M, Chandel NS (2014) ROS function in redox signaling and oxidative stress. Curr Biol 24:R453-62. https://doi.org/10.1016/j.cub.2014.03.034

715 Shahabadi N, Mirzaei Kalar Z, Hosseinpour Moghadam N (2012) DNA interaction studies of a
716 platinum (II) complex containing an antiviral drug, ribavirin: The effect of metal on DNA
717 binding. Spectrochim Acta A Mol Biomol Spectrosc 96:723–728.
718 https://doi.org/10.1016/j.saa.2012.07.020

719 Shawe-Taylor M, Greenwood D, Hobbs A, et al (2024) Divergent performance of vaccines in the
720 UK autumn 2023 COVID-19 booster campaign. The Lancet 403:1133–1136.
721 https://doi.org/10.1016/S0140-6736(24)00316-7

722 Shi Y, Wang Y, Shao C, et al (2020) COVID-19 infection: the perspectives on immune responses.
723 Cell Death Differ 27:1451–1454

724 Shionoiri N, Sato T, Fujimori Y, et al (2012) Investigation of the antiviral properties of copper
725 iodide nanoparticles against feline calicivirus. J Biosci Bioeng 113:580–586.
726 https://doi.org/10.1016/j.jbiosc.2011.12.006

727 Teyssot M-L, Jarrousse A-S, Manin M, et al (2009) Metal-NHC complexes: a survey of anti-
728 cancer properties. Dalton Transactions 6894. https://doi.org/10.1039/b906308k

729 Thakur V, Ratho RK (2021) OMICRON (B.1.1.529): A new SARS-CoV-2 variant of concern
730 mounting worldwide fear. J Med Virol. https://doi.org/10.1002/jmv.27541

731 Tomasi J, Mennucci B, Cammi R (2005) Quantum Mechanical Continuum Solvation Models.
732 Chem Rev 105:2999–3094. https://doi.org/10.1021/cr9904009

733 V'kovski P, Kratzel A, Steiner S, et al (2021) Coronavirus biology and replication: implications
734 for SARS-CoV-2. Nat Rev Microbiol 19:155–170. https://doi.org/10.1038/s41579-020-
735 00468-6

736 von Delft A, Hall MD, Kwong AD, et al (2023) Accelerating antiviral drug discovery: lessons
737 from COVID-19. Nat Rev Drug Discov 22:585–603. https://doi.org/10.1038/s41573-023-
738 00692-8

739 Wang P, Wang M, Yu J, et al (2021) Increased Resistance of SARS-CoV-2 Variant P.1 to
740 Antibody Neutralization. bioRxiv 2021.03.01.433466.
741 https://doi.org/10.1101/2021.03.01.433466

742 Weigend F, Ahlrichs R (2005) Balanced basis sets of split valence, triple zeta valence and
743 quadruple zeta valence quality for H to Rn: Design and assessment of accuracy. Physical
744 Chemistry Chemical Physics 7:3297. https://doi.org/10.1039/b508541a

745 Yong SJ (2021) Long COVID or post-COVID-19 syndrome: putative pathophysiology, risk
746 factors, and treatments. Infect Dis 53:737–754.
747 https://doi.org/10.1080/23744235.2021.1924397

748 Zeng C, Evans JP, King T, et al (2022) SARS-CoV-2 spreads through cell-to-cell transmission.
749 Proceedings of the National Academy of Sciences 119:.
750 https://doi.org/10.1073/pnas.2111400119

751 Zhang T, Wu Q, Zhang Z (2020) Probable Pangolin Origin of SARS-CoV-2 Associated with the
752 COVID-19 Outbreak. Current Biology 30:1346-1351.e2.
753 https://doi.org/10.1016/j.cub.2020.03.022

754 Zoroddu MA, Aaseth J, Crisponi G, et al (2019) The essential metals for humans: a brief
755 overview. J Inorg Biochem 195:120–129. https://doi.org/10.1016/j.jinorgbio.2019.03.013

756

## FIGURE CAPTIONS

**Figure 1: Chemical structure of Cu(IPr)Cl, Cu(IMes)Cl and, $Cu(IMes)_2BF_4$** (Fontes et al. 2022)

**Figure 2. Dose-response curve for Cu(IPr)Cl (A), Cu(IMes)Cl (B), and $[Cu(IMes)_2]BF_4$ (C) treatment on A549-AT cells in the presence of absence of SARS-CoV-2-mNeongreen**. A549-AT cells were treated with the Cu(IPr)Cl, Cu(IMes)Cl, or $[Cu(IMes)_2]BF_4$ at concentrations ranging from 0.58 µM to 300 µM, in a two-fold serial dilution in the presence of absence of SARS-CoV-2-mNeongreen at a MOI of 0.1. After 24h, the efficiency of infection was revealed by measurement of the total integrated intensity of the fluorescence (GCU x $\mu m^2$/well) using the IncuCyte S3 microscope. Cell viability was accessed by MTT assay. Mean values of two independent experiment each measured in quadruplicate including the standard deviation are shown. **(D) C**ytotoxic concentration at 50% ($CC_{50}$), effective concentration at 50% (EC50) and Selective Indexes of compounds are reported. All images were generated using GraphPad Prism 10 and Adobe Illustrator 2024 (version 28.5).

**Figure 3. Pre-treatment with Cu(IMes)Cl and $Cu(IMes)_2BF_4$ protects A549-AT cells against SARS-CoV-2 infection.** (A) Schematic representation of each time-based assay as indicated by A549-AT cells (blue arrows), compounds (chemical structure), and SARS-CoV-2-mNeonGreen (green virus). (B) Virus inhibition was analysed as described for Fig. 2. Mean values ± SD of a minimum of three independent experiments each measured in quadruplicate. Statistical comparison performed with One-way ANOVA - Dunett test in which (ns) non-significant and (****) $P < 0.001$. All images were generated using GraphPad Prism 10 and Adobe Illustrator 2024 (version 28.5).

**Figure 4. Cu(I) complexes impair several stages of SARS-CoV-2 entry**. (A and B) A549-AT cells were infected with SARS-CoV-2-mNeonGreen (MOI 1) and simultaneously treated Cu(IPr)Cl, Cu(IMes)Cl, and $[Cu(IMes)_2]BF_4$ for 1 h. Cells were washed and replaced by fresh medium. (C and D) SARS-CoV-2-mNeonGreen (MOI 5) and each compound was incubated for 1 h at 37 °C and then for one extra hour with the cells. Then, virus and compound were removed, cells were washed with PBS, and added fresh medium. (E and F) A549-AT cells were infected with the virus and simultaneously treated with each compound for 1 h at 4 °C. The cells were washed to remove virus and compound and replaced with fresh medium. (G and H) A549-AT cells were infected with virus and simultaneously treated with the compounds for 1 h at 4 °C. For each of assay the measurement of virus infection was performed as described for Fig. 2. Schematic representation of each time-based assay as indicated by A549-AT cells (blue arrows), compounds (chemical structure), and SARS-CoV-2-mNeonGreen (green virus), SARS-CoV-2-mNeonGreen and compound inoculum (microtube), incubation at 4°C (ice crystal) and incubation at 37°C (thermometer). Mean values ± SD of a minimum of three independent experiments each measured in quadruplicate. Statistical comparison performed with One-way ANOVA - Dunett test in which (****) $P < 0.0001$. All images were generated using GraphPad Prism 10 and Adobe Illustrator 2024 (version 28.5).

**Figure 5. Cu(IPr)Cl, Cu(IMes)Cl, and $[Cu(IMes)_2]BF_4$ potently impair post-entry stages of SARS-CoV-2 replication**. A549-AT cells were infected with SARS-CoV-2-mNeonGreen (MOI 0.1) for 1h (A) or for 6h (B), and then treated with each complex for the remaining 24h. Schematic representation of each time-based assay as indicated by A549-AT cells (blue arrows), compounds (chemical structure), and SARS-CoV-2-mNeonGreen (green virus). For each treatment the measurement of virus infection was performed as described for Fig. 2. Mean values ± SD of a minimum of three independent experiments each measured in triplicate. Statistical comparison performed with One-way ANOVA - Dunett test in which (****) $P < 0.0001$. All images were generated using GraphPad Prism 10 and Adobe Illustrator 2024 (version 28.5).

**Figure 6. Effect of Cu(IPr)Cl, Cu(IMes)Cl, and $[Cu(IMes)_2]BF_4$ against SARS-CoV-2-Wuhan-B.1.617.2-Spike and SARS-CoV-2-Wuhan-BA.2-Spike chimeras.** (A) Schematic representation of the icDNAs of the Wuhan strain (NCBI: NC_045512.2) (1) and chimeric variants SARS-CoV-2-Wuhan-B.1.617.2-Spike (2) and SARS-CoV-2-Wuhan-BA.2-Spike (3) that also carry mCherry reporter. (B, C). A549-AT cells were infected with SARS-CoV-2-Wuhan-B.1.617.2-Spike (B) or SARS-CoV-2-Wuhan-BA.2-Spike (C) at an MOI of 0.1 in the absence of presence of indicated compounds for 24h. SARS-CoV-2 replication was measured by the total integrated intensity of the red fluorescence (RCU x $\mu m^2$/well). Statistical comparison performed with One-way ANOVA - Dunett test in which (****) $P < 0.0001$. All images were generated using GraphPad Prism 10 and Adobe Illustrator 2024 (version 28.5).

**Figure 7. Effect of the Cu(I)(NHC) against the patient-isolated SARS-CoV-2-B.1.617.2 and SARS-CoV-2-BA.2 replication.** A549-AT cells were infected with SARS-CoV-2-B.1.617.2 (A) or SARS-CoV-2-BA.2 (B) at an MOI of 0.1 in the presence of each compound for 24h. Then, supernatant was collected and tittered by $TCID_{50}$. Statistical comparison performed with One-way ANOVA - Dunett test in which (****) $P < 0.0001$. All images were generated using GraphPad Prism 10 and Adobe Illustrator 2024 (version 28.5).

**Figure 8. Cu(I)(NHC) compounds interaction with SARS-CoV-2 proteases.** The inhibition concentration of 50% ($IC_{50}$) of Cu(IMes)Cl against SARS-CoV-2 $PL^{pro}$ (A) and Cu(IMes)Cl and $[Cu(IMes)_2]BF_4$ against SARS-CoV-2 $M^{pro}$ (B) is shown. Further, the representation of the active site from $PL^{pro}$ highlighting the main residues, drug binding domain (square), the catalytic triad of hydrolysis(circle), residues interaction from the best docking poses of Cu(IMes)Cl and $PL^{pro}$ as well as Cu(IMes)Cl and $[Cu(IMes)_2]BF_4$ with SARS-CoV-2 $M^{pro}$ is shown in C and D, respectively.

**Figure 9. $[Cu(IMes)_2]BF_4$ decreases SARS-CoV-2 cell to cell spread.** A549-AT cells were infected with SARS-CoV-2-mNeonGreen (MOI 0.05) for 1h, cells were washed, and replaced by fresh medium containing each compound and Methylcellulose 0.8% for the remaining 48h. The photos were taken by the IncuCyte S3 microscope in the objective 10x under the green fluorescence light and focus size analysis were performed in ImageJ. (A) Representative images of SARS-CoV-2-mNeonGreen infection in the presence of DMSO control, $[Cu(IMes)_2]BF_4$, and methylcellulose negative ($MC^-$) control, in this order. (B) The average focus area (in $\mu M^2$) of three technical repeats is shown. Statistical comparison performed with One-way ANOVA – Holm-Sidak test in which (**) $P < 0.01$.

All images were generated using GraphPad Prism 10 and Adobe Illustrator 2024 (version 28.5).

# Cu(I)-N-HETEROCYCLIC CARBENES

AS POTENT INHIBITORS OF

## SARS-COV-2 REPLICATION

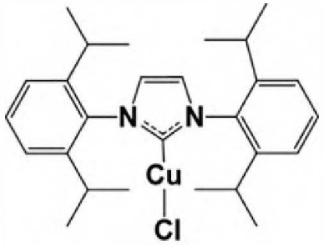


[Cu(IPr)Cl]

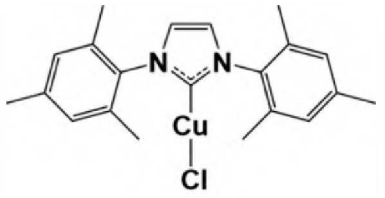


[Cu(IMes)Cl]

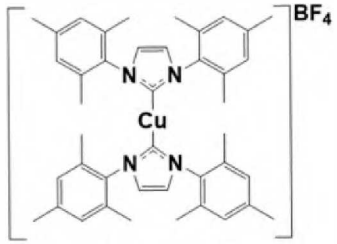


$[Cu(IMes)_2]BF_4$

## OUR MAIN FINDINGS

Selectivity indexes of 11.23, 10.84, and 5.94

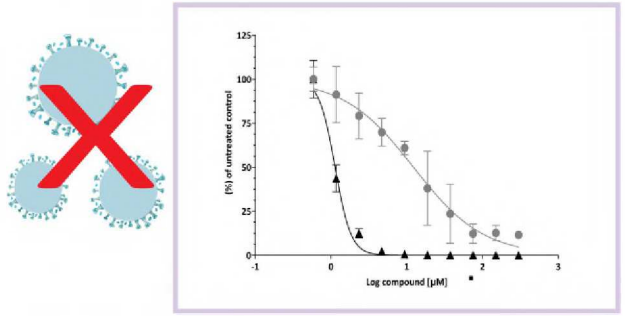


Cu(Imes)Cl inhibits PLpro protease activity

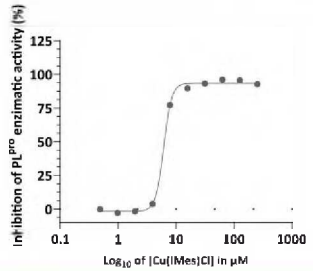


$Cu(IMes)_2BF_4$ impairs cell to cell spread

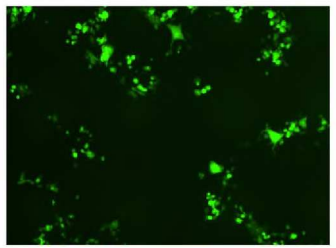

Molecular docking interaction with PLpro

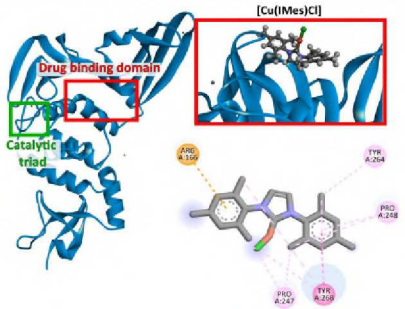


Cu(I)-N-Heterocyclic carbenes inhibits SARS-CoV-2 Delta and Omicron variants

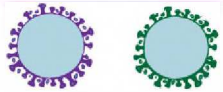

B.1.617.2 BA.2

## CONCLUSIONS

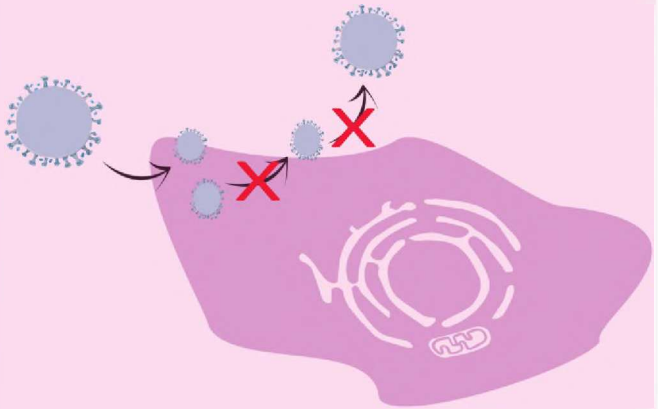

Cu(IMes)Cl and $[Cu(IMes)_2]BF_4$ show strong antiviral activity against SARS-CoV-2, including its variants B.1.617.2 and BA.2.

These findings highlight the potential of Cu(NHC) compounds for antiviral therapy and encourage further pre-clinical studies, particularly for Cu(IMes)Cl.

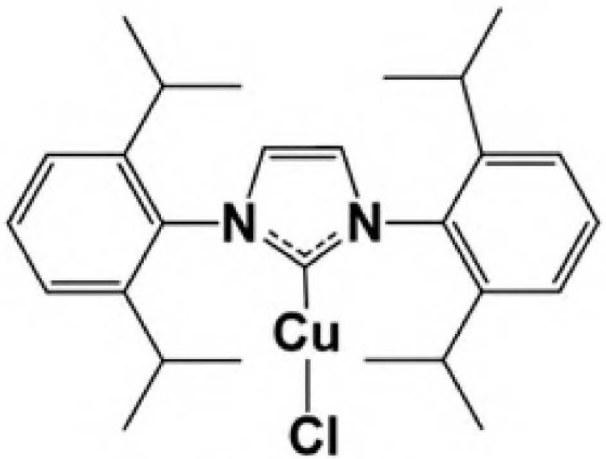


[Cu(IPr)Cl]

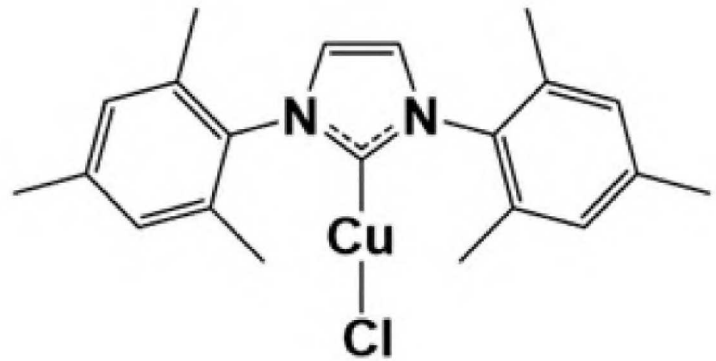


[Cu(IMes)Cl]

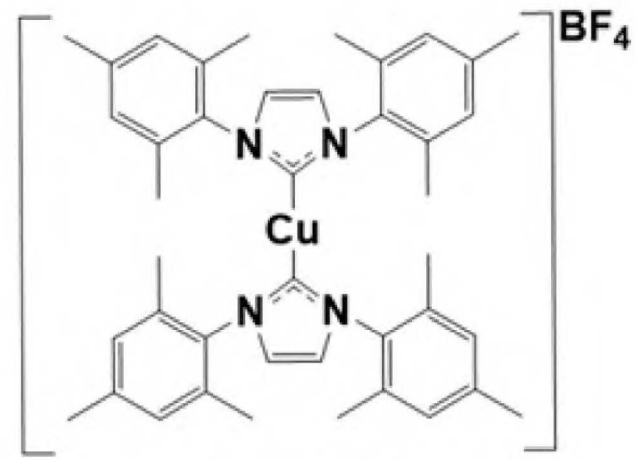


$[Cu(IMes)_2]BF_4$

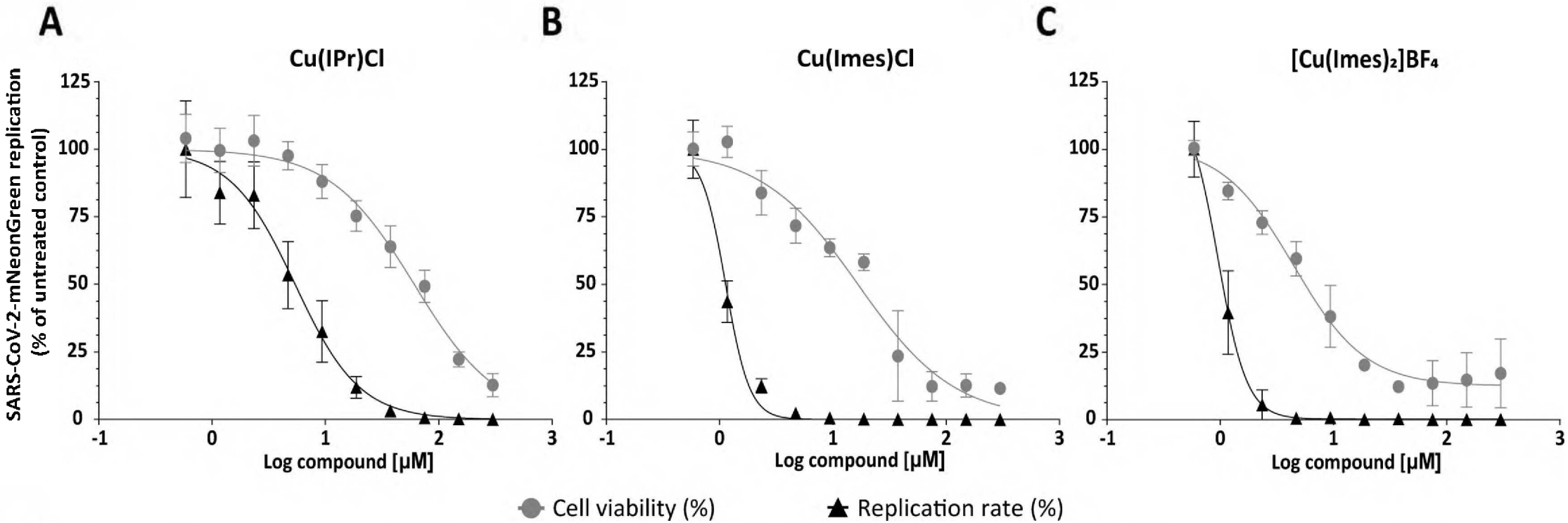


D

| COMPOUND | CYTOTOXIC CONCENTRATION OF 50% ($CC_{50}$ - µM) | EFFECTIVE CONCENTRATION OF 50% ($EC_{50}$ - µM) | SELECTIVE INDEX (SI) |
|---|---|---|---|
| Cu(Ipr)Cl | 60.68 ± 3.95 | 5.40 ± 2.20 | 11.23 |
| Cu(Imes)Cl) | 12.26 ± 5.75 | 1.13 ± 0.08 | 10.84 |
| $[Cu(Imes)_2]BF_4$ | 6.48 ± 0.56 | 1.09 ± 0.11 | 5.94 |

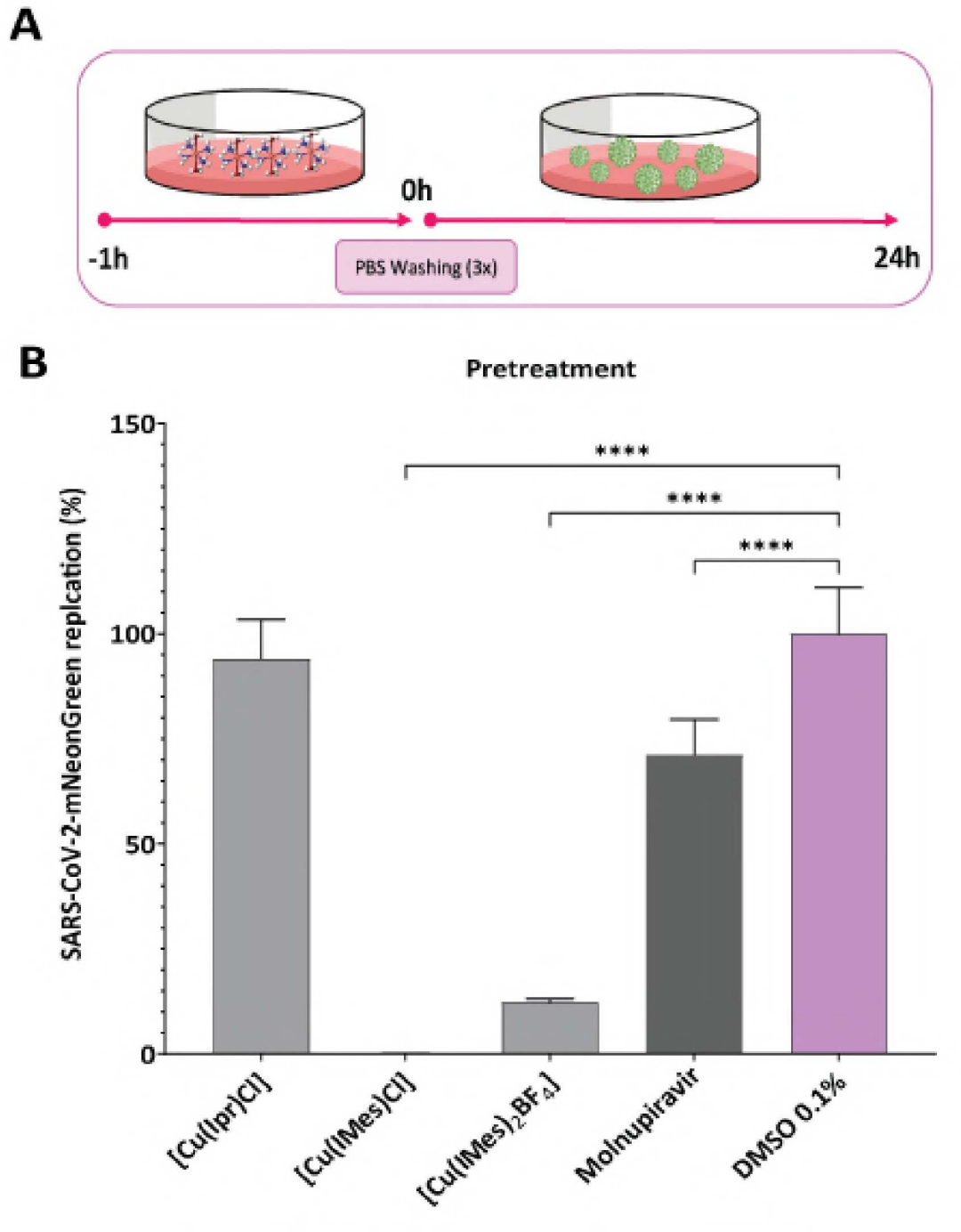
A
0h
-1h
PBS Washing (3x)
24h
B
Pretreatment
SARS-CoV-2-mNeonGreen replcation (%)
150
100
50
0
****
****
****
[Cu(Ipr)Cl]
[Cu(IMes)Cl]
[Cu(IMes)2BF4]
Molnupiravir
DMSO 0.1%

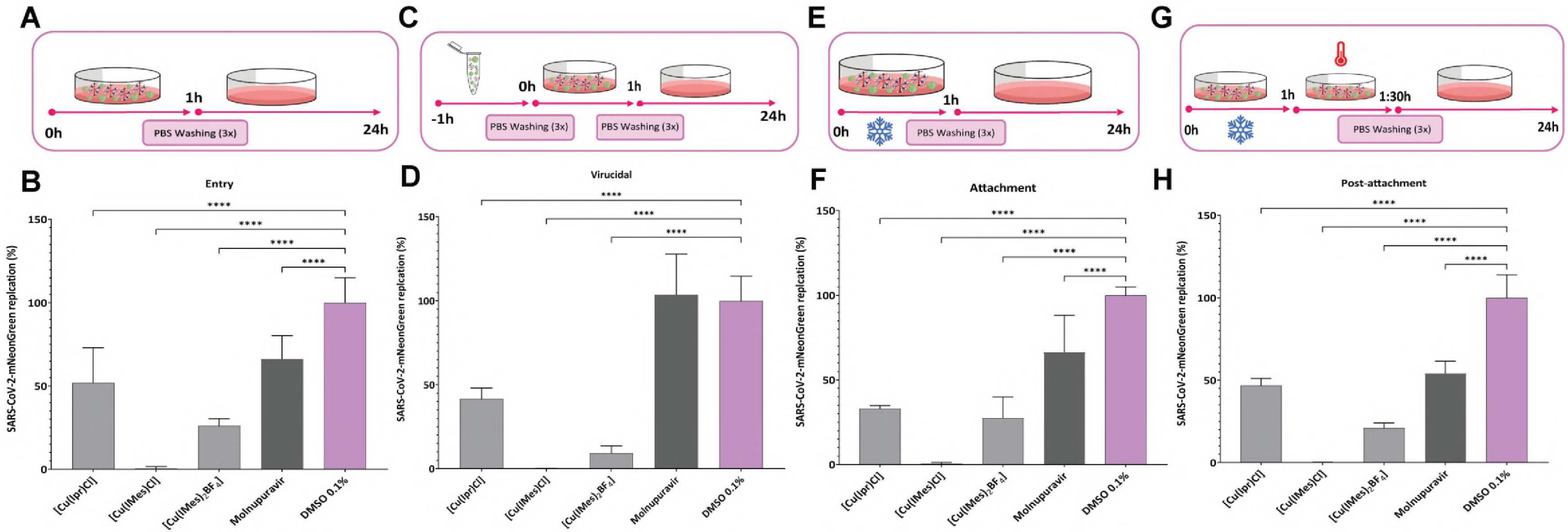
A
0h
1h
PBS Washing (3x)
24h
C
-1h
0h
1h
PBS Washing (3x)
PBS Washing (3x)
24h
E
0h
1h
PBS Washing (3x)
24h
G
0h
1h
1:30h
PBS Washing (3x)
24h
B
Entry
D
Virucidal
F
Attachment
H
Post-attachment
SARS-CoV-2-mNeonGreen replcation (%)
0
50
100
150
****
[Cu(Ipr)Cl]
[Cu(IMes)Cl]
[Cu(IMes)2BF4]
Molnupuravir
DMSO 0.1%

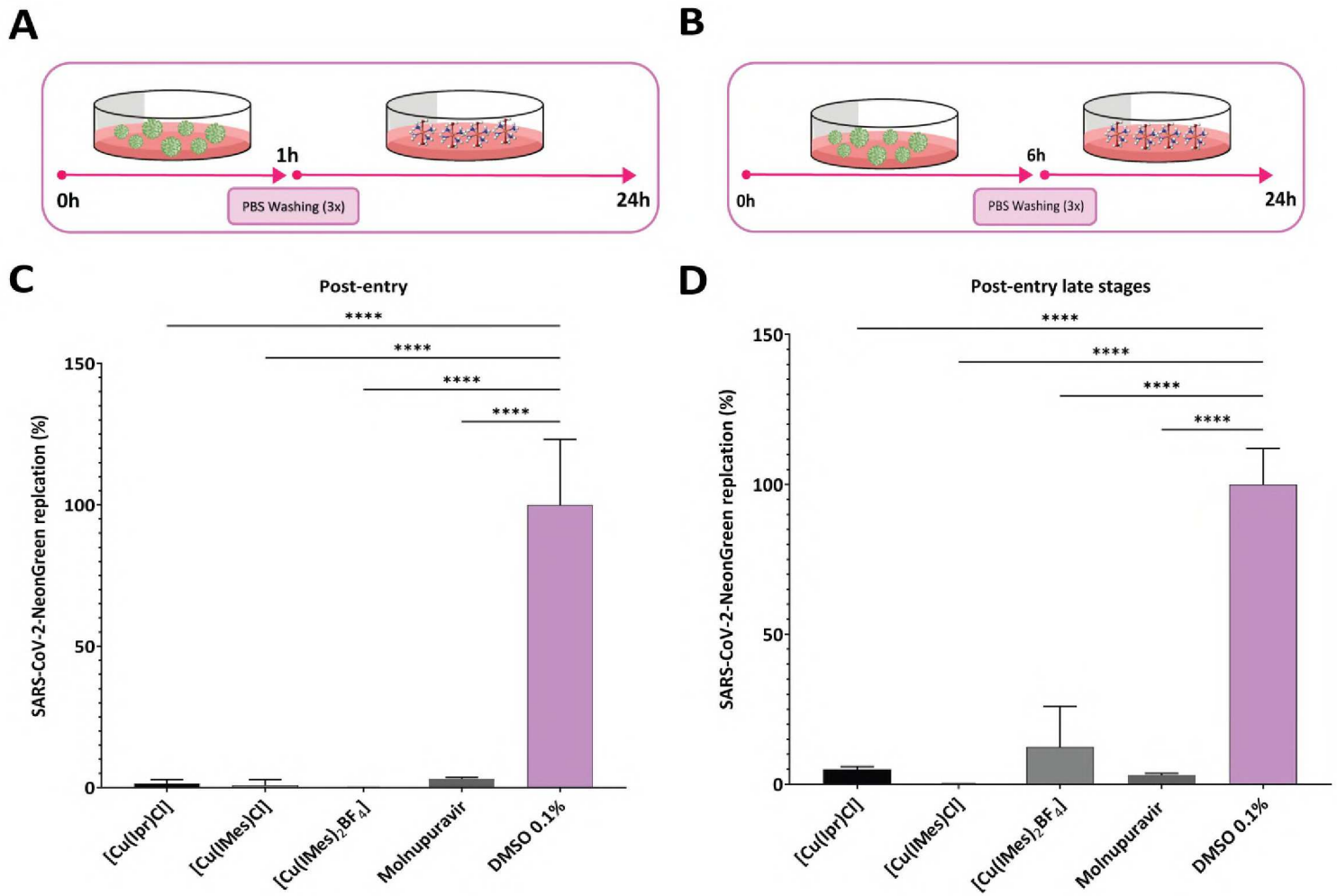
A
1h
0h
PBS Washing (3x)
24h
B
6h
0h
PBS Washing (3x)
24h
C
Post-entry
SARS-CoV-2-NeonGreen replcation (%)
150
100
50
0
****
****
****
****
[Cu(Ipr)Cl]
[Cu(IMes)Cl]
[Cu(IMes)2BF4]
Molnupuravir
DMSO 0.1%
D
Post-entry late stages
SARS-CoV-2-NeonGreen replcation (%)
150
100
50
0
****
****
****
****
[Cu(Ipr)Cl]
[Cu(IMes)Cl]
[Cu(IMes)2BF4]
Molnupuravir
DMSO 0.1%

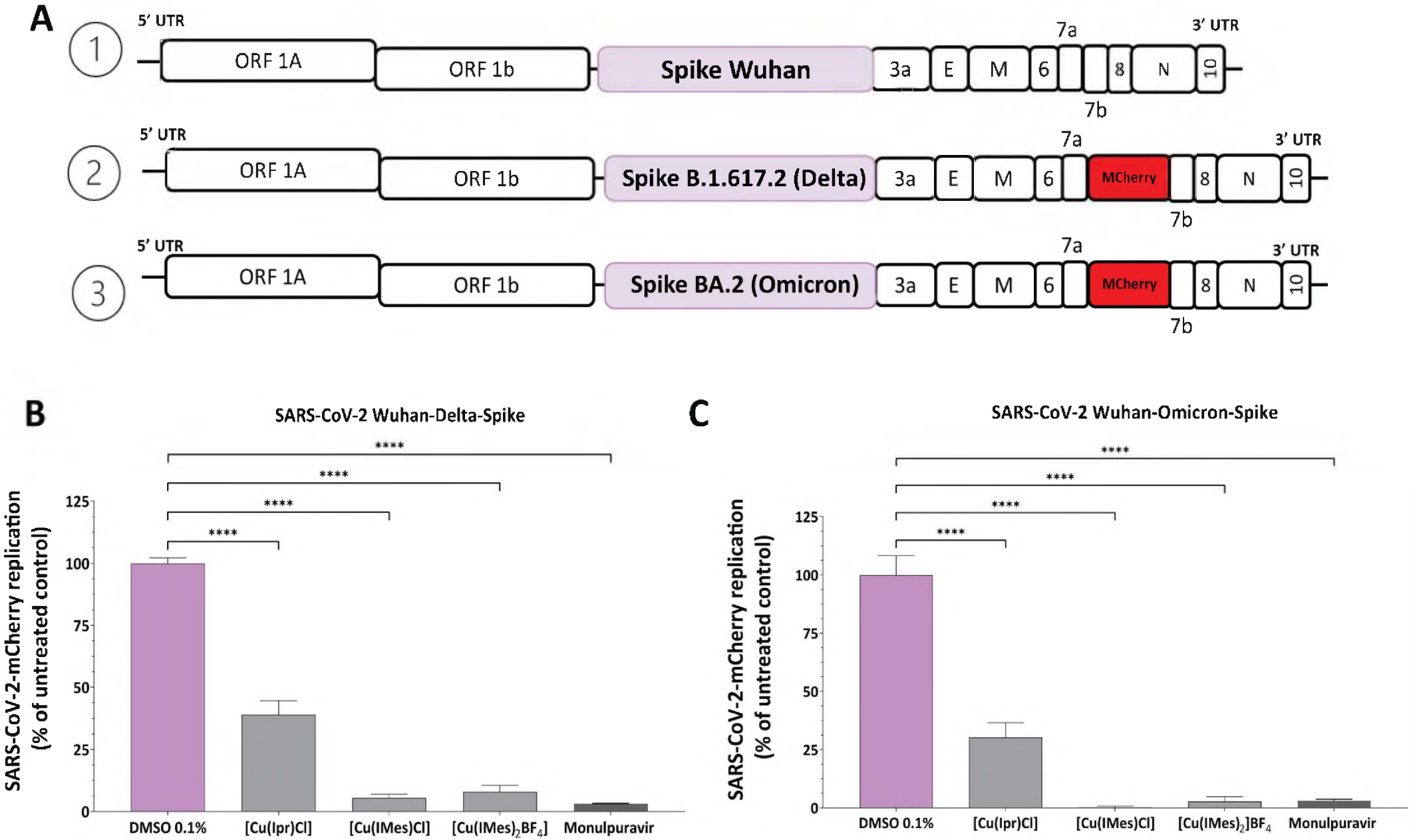
A
1
5' UTR
ORF 1A
ORF 1b
Spike Wuhan
3a
E
M
6
7a
7b
8
N
10
3' UTR
2
5' UTR
ORF 1A
ORF 1b
Spike B.1.617.2 (Delta)
3a
E
M
6
7a
MCherry
7b
8
N
10
3' UTR
3
5' UTR
ORF 1A
ORF 1b
Spike BA.2 (Omicron)
3a
E
M
6
7a
MCherry
7b
8
N
10
3' UTR
B
SARS-CoV-2 Wuhan-Delta-Spike
SARS-CoV-2-mCherry replication
(% of untreated control)
****
****
****
****
125
100
75
50
25
0
DMSO 0.1%
[Cu(Ipr)Cl]
[Cu(IMes)Cl]
[Cu(IMes)2BF4]
Monulpuravir
C
SARS-CoV-2 Wuhan-Omicron-Spike
SARS-CoV-2-mCherry replication
(% of untreated control)
****
****
****
****
125
100
75
50
25
0
DMSO 0.1%
[Cu(Ipr)Cl]
[Cu(IMes)Cl]
[Cu(IMes)2]BF4
Monulpuravir

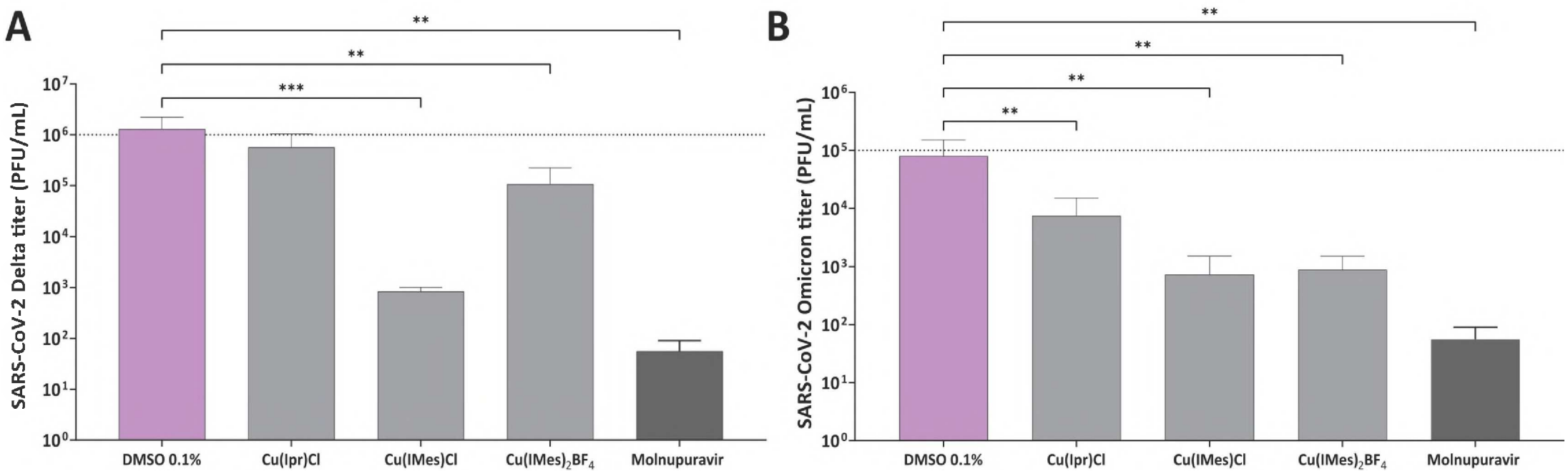
A
SARS-CoV-2 Delta titer (PFU/mL)
$10^7$
$10^6$
$10^5$
$10^4$
$10^3$
$10^2$
$10^1$
$10^0$
**
**
***
DMSO 0.1%
Cu(Ipr)Cl
Cu(IMes)Cl
Cu(IMes)$_2$BF$_4$
Molnupuravir
B
SARS-CoV-2 Omicron titer (PFU/mL)
$10^6$
$10^5$
$10^4$
$10^3$
$10^2$
$10^1$
$10^0$
**
**
**
**
DMSO 0.1%
Cu(Ipr)Cl
Cu(IMes)Cl
Cu(IMes)$_2$BF$_4$
Molnupuravir

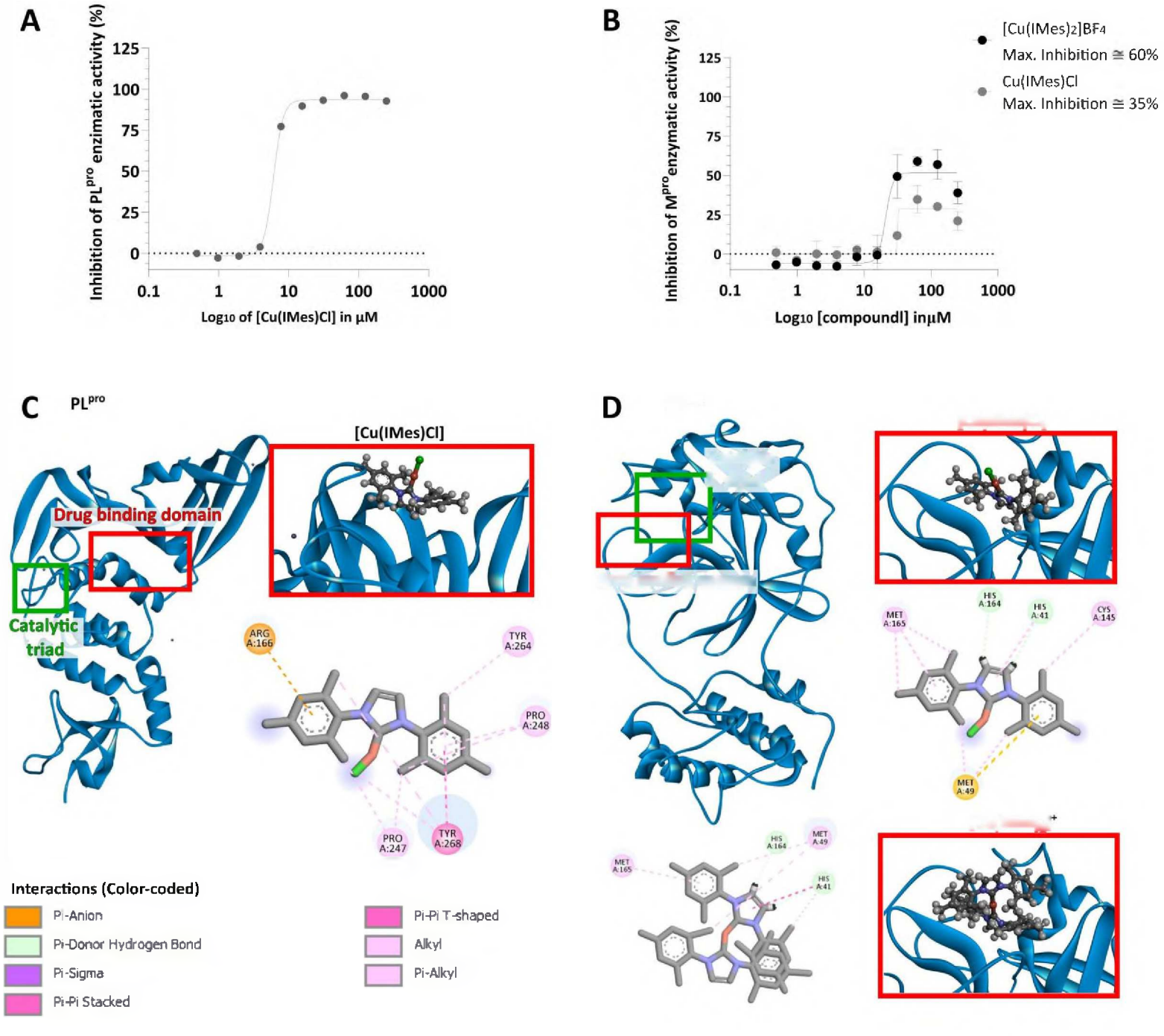
A
Inhibition of PL^pro enzimatic activity (%)
125
100
75
50
25
0
0.1
1
10
100
1000
Log10 of [Cu(IMes)Cl] in µM
B
Inhibition of M^pro enzymatic activity (%)
[Cu(IMes)2]BF4
Max. Inhibition ≅ 60%
Cu(IMes)Cl
Max. Inhibition ≅ 35%
Log10 [compoundl] inµM
C
PL^pro
[Cu(IMes)Cl]
Drug binding domain
Catalytic triad
ARG A:166
TYR A:264
PRO A:248
PRO A:247
TYR A:268
Interactions (Color-coded)
Pi-Anion
Pi-Donor Hydrogen Bond
Pi-Sigma
Pi-Pi Stacked
Pi-Pi T-shaped
Alkyl
Pi-Alkyl
D
HIS A:164
HIS A:41
CYS A:145
MET A:165
MET A:49